Cell attachment and tail contraction of *S. aureus* phage phi812

Ján Bíňovský[1,2]*, Marta Šiborová[1]*, Jiří Nováček[1], Pavol Bárdy[3], Roman Baška[1], Karel Škubník[1], Tibor Botka[3], Martin Benešík[3], Roman Pantůček[3], Konstantinos Tripsianes[1], Pavel Plevka[1]

[1] *Central European Institute of Technology, Kamenice 753/5, 625 00 Brno, Czech Republic*

[2] *National Centre for Biomolecular Research, Faculty of Science, Masaryk University, 625 00, Brno, Czech Republic*

[3] *Faculty of Science, Masaryk University, Kamenice 753/5, 625 00 Brno, Czech Republic*

** These authors contributed equally to this work*

Abstract

Phages with contractile tails employ elaborate strategies to penetrate bacterial cell walls and deliver their genomes into the host cytoplasm. Most tailed phages that have been structurally characterized to date infect Gram-negative bacteria, but those targeting Gram-positive bacteria, many of which are important human pathogens, are less well understood. Here, we show that the baseplate of phage phi812, which infects Gram-positive *Staphylococcus aureus*, is formed of a core, wedge modules, and baseplate arms carrying receptor-binding proteins type 1 and 2 and tripod complexes. Upon binding to the *S. aureus* cell wall, the symmetry of the baseplate transforms from threefold to sixfold. The conformational changes propagate from the outer edge to the core of the baseplate. The receptor-binding proteins re-orient to bind to the host cell. Subsequently, central spike proteins degrade teichoic acids. The conformational changes to the tripod complexes trigger the release of the central spike and weld proteins from the baseplate, which enables the hub proteins to cleave cell wall peptidoglycan and facilitate penetration of the tail tube tip through the cell membrane. Changes in the positions of baseplate arms are transmitted through wedge modules to tail sheath initiator proteins. The ring formed by the tail sheath initiator proteins expands in diameter and thus triggers the contraction of the tail sheath. The tail sheath of phi812, which can bend up to 90° in its native conformation, shortens from 200 to 96 nm, which pushes the tail tube 10-30 nm into the cytoplasm, depending on the local thickness of the *S. aureus* cell wall. Our results provide the foundation for engineering phi812 to target specific *S. aureus* strains.

Introduction

Tailed phages use baseplates at the end of their tails to attach to the host cell surface to initiate infection[1]. The cell binding of phages with contractile tails is coupled with a conformational change to the baseplate that triggers tail sheath contraction[2]. The tail tube penetrates the cell wall and enables the ejection of the phage genome into the bacterial cytoplasm. Most of the phages with contractile tails and CISs structurally characterized to date attack Gram-negative bacteria[3–9]. Current knowledge regarding the mechanisms that are employed to breach the cell wall of Gram-positive bacteria is limited.

Phages of the genus *Kayvirus* of the family *Herelleviridae* exhibit high lytic activity against Gram-positive bacterium *Staphylococcus aureus*[10]. This human pathogen can cause skin and epithelial infections, as well as bacteremia that can develop into life-threatening sepsis[11,12]. *S. aureus* is frequently resistant to antibiotics, which has renewed interest in phage therapy[13–15]. The best studied *Kayvirus*, phage K, shares 98.5% of the genome identity with a polyvalent phage phi812. Host range mutants of phage phi812 were shown to infect more than 90 % of *Staphylococcus aureus* isolates[10,16].

It has been shown that a virion of phi812 is formed by an icosahedral head with a diameter of 90 nm and a 240-nm-long tail that ends with a lentil-shaped baseplate[17]. Upon binding to the *S. aureus* cell wall, the baseplate transforms into a double-layered disc-shaped conformation. Furthermore, the structure of phage A511 of the *Herelleviridae* family, which infects Gram-positive *Listeria* and is morphologically similar to phi812, has also been determined[18]. However, the resolutions of the previous studies of phi812 and A511 were limited to 13 and 14 Å, respectively, which prevented the identification of some of the baseplate components and characterization of their conformational changes that enable cell wall binding, tail contraction, and genome delivery.

The naming convention for baseplate components was established in the pioneering studies of phage T4. The core of the baseplate is formed by central hub[3,19], which serves as a centerpiece for the baseplate assembly and a platform for the tail tube polymerization. Six wedge complexes encircle the core and provide foundation for tail sheath assembly[3,19]. Baseplate core proteins of contractile-tailed phages exhibit a high degree of structural conservation[3,19,20]. In addition, the structures of the baseplate core proteins are shared by contractile injection systems (CISs)[21–27]. The outer baseplate of contractile-tailed phages can be either simple, containing one or two tail fibers to bind to host cellular receptors[4–9], or more intricate, such as that of T4[3].

Here, we used a combination of cryo-EM, X-ray crystallography, nuclear magnetic resonance spectroscopy (NMR), and AlphaFold2 predictions to build the molecular structure of the phi812 baseplate in native and cell-bound conformations. The phi812 baseplate contains more than one hundred predicted receptor-binding sites for attachment to the *S. aureus* cell wall. Based on comparing the native and contracted structures, we propose a sequence of conformational changes that propagate from the baseplate periphery to the core and trigger the tail sheath contraction. Enzymes degrading teichoic acid and peptidoglycan attached to the tail tube tip facilitate its penetration through the *S. aureus* cell wall.

Results and Discussion

The native structure of phi812 baseplate

The structure of the phi812 baseplate with imposed sixfold symmetry was previously determined to a resolution of 13 Å using cryo-EM[17]. However, here we show that the phi812 baseplate, similar to that of A511[18], is only approximately sixfold symmetric. Reduction of the symmetry of the reconstruction to threefold enabled the determination of the overall baseplate structure to a resolution of 7.3 Å (Fig. 1A, B, SFig. 1, 2A and 3, Table S1). The baseplate of phi812 is lentil-shaped with a diameter of 655 Å and height of 310 Å, and can be divided into a core, six wedge modules, and six arms decorated with three types of receptor-binding proteins (Fig. 1). A localized reconstruction of the baseplate core and wedge modules reached a resolution of 4.4 Å, which enabled the determination of the structures of the tail tube initiator, tail sheath initiator, hub, assembly, central spike, weld, wedge, and arm scaffold proteins (Fig. 1C, D, SFig. 1, 2B, C and 3, SMovie 1). The hexamer of tail tube initiator proteins (gp113) and trimer of hub proteins (gp110) form a channel, which extends the tail tube channel into the baseplate. The trimer of central spike proteins (gp112), bound to the three copies of weld protein (gp111), plugs the baseplate channel at the level of the hub proteins (Fig. 1D). The hexamer of tube initiator proteins is surrounded by six copies of each of the sheath initiator (gp115) and assembly proteins (gp114), which are placed above each other (Fig. 1C, D, and 2). The baseplate core is encircled by the six wedge modules, which enable the attachment of baseplate arms (Fig. 1C, D, and 2, SMovie 1). Each wedge module is a heterotrimer formed by two copies of wedge protein (gp116) and an N-terminal part of the arm scaffold protein (gp117) (Fig. 1C and 2, SMovie 1). One rod-shaped baseplate arm protrudes radially from each wedge module (Fig. 1A, B, SMovie 2). The baseplate arm is formed by the C-terminal extended part of the arm scaffold protein reinforced by three dimers of the arm segment protein (gp118) (Fig. 1B and 3A-C, SFig. 4). The arm scaffold protein provides attachment sites for two trimers of the tripod proteins (gp119), a trimer of receptor-binding protein 1 (RBP1, gp121), and a trimer of receptor-binding protein 2 (RBP2, gp123) (Fig. 1A, B, SMovie 2). The trimer of tripod proteins located closer to the tail axis (inner tripod) is oriented with its receptor-binding domains pointing away from the phage head (Fig. 1A, B). In contrast, the receptor-binding domains of tripod proteins attached to the baseplate arm further away from the tail axis (outer tripod) point towards the phage head (Fig. 1B). Trimers of RBP1 and RBP2 are attached to the end of the baseplate arm (Fig. 1A, B). The RBP1 reaches from one baseplate arm to the neighboring one, where it interacts with RBP2 (Fig. 1A, SFig. 5A, B). The RBP2 points towards the tail sheath (Fig. 1A, B, SFig. 5).

The deviation of the phi812 baseplate from sixfold symmetry is most apparent in the distinct conformations of the alternating baseplate arms and the positions of the receptor-binding proteins attached to them (Fig. 1A, B, SMovie 2). The six inner tripods form the shape of an equilateral triangle when viewed along the tail axis towards the phage head (Fig. 1A). The center of mass of the inner tripod positioned at the triangle vertex is 141 Å from the tail axis, whereas that forming the edge is 87 Å from the tail axis (Fig. 1A). The differences in the positioning of the tripods are caused by the alternating arrangement of baseplate arms that point away from the tail axis at different angles (Fig. 1B). The inner tripods at the vertices are attached to upper baseplate arms that radiate from the tail axis at an angle of 72 ° (Fig. 1B). In contrast, the inner tripods forming the triangle edges are attached to the lower baseplate arms radiating at an angle of 62 ° (Fig. 1B). The distinct directions of the baseplate arms also influence the interactions of proteins at the baseplate

116 periphery. The outer tripod and RBP2 attached to the upper baseplate arm interact with a wedge
117 protein and the first tail sheath disc (Fig. 1B, SFig. 5B, D). In contrast, the RBP2 bound to the lower
118 baseplate arm only contacts a wedge protein, and the corresponding outer tripod does not interact
119 with the tail sheath (Fig. 1B, SFig. 5A, C). We speculate that the native structure of the phi812
120 baseplate with overall threefold symmetry is established during the baseplate formation and is
121 determined by the structure of the trimer of hub proteins (Fig. 1D and 2). The two wedge modules
122 that attach to each hub protein differ in their positioning relative to the tail axis (Fig. 1D, SFig. 6A-C,
123 SMovie 1). These structural differences propagate into the baseplate periphery, resulting in the
124 alternating angles of the baseplate arms relative to the tail axis (Fig. 1B, SMovie 2). The same
125 mechanism is probably employed to establish the threefold symmetry of the A511 baseplate[18]. In
126 contrast, baseplate core proteins of recently characterized phages were shown to be arranged with
127 quasi-sixfold symmetry[3–9].
128

129 **Central spike protein blocks the baseplate channel and degrades teichoic acid**

130 The trimer of central spike proteins of phi812 blocks the baseplate channel and protrudes ~22 nm
131 from the baseplate (Fig. 1B, D and 4A, B, SMovie 2). The central spike protein can be divided into
132 oligosaccharide-binding, β-prism, coiled-coil, knob, and petal domains (Fig. 2, SFig. 7A). The
133 oligosaccharide-binding and β-prism domains have conserved structures shared by central spike
134 proteins of other phages and CISs [4,6–9,22–26]. The two domains bind to the inside of the channel formed
135 by the hub proteins (Fig. 1D and 2). The coiled-coil, knob, and petal domains protrude from the
136 phi812 baseplate and are not resolved in the cryo-EM reconstruction of the baseplate, due to the
137 coiled-coil domain's flexibility (Fig. 1B and 4A, B). Structural prediction indicates that the coiled-coil
138 domains from the three central spike proteins form a 22-nm-long fiber (Fig. 2). The structures of the
139 knob and petal domains were determined by cryo-EM and single-particle reconstruction of a
140 recombinantly produced central spike protein (Fig. 1B and 4C, SFig. 1, 2J and 3, Table S1). The knob
141 domain has a tumor necrosis factor-like fold[28], similar to that of the head domains of
142 receptor-binding proteins from lactococcal phages Tuc2009 and 1358[29–31] and a lectin from
143 *Burkholderia cenocepacia*[32] which indicates that the knob domain may bind to saccharides from the
144 bacterial cell wall (SFig. 7A, Table S2). The petal domain of the central spike protein has an α/β-barrel
145 fold, and is structurally similar to the protein GlpQ from *B. subtilis* that cleaves teichoic acid during
146 phosphate starvation[33,34] (Fig. 4C, SFig. 7A, Table S2).
147 Phages with contractile tails and CISs attacking Gram-negative bacteria pierce the outer
148 bacterial membranes using puncturing tips formed of proteins with β-prism or β-helix domains[35–37].
149 In contrast, to infect Gram-positive *S. aureus*, phage phi812 has to penetrate a 50-70-nm-thick layer
150 of teichoic acids and peptidoglycan. Therefore, we propose that the knob and petal domains of the
151 central spike of phi812 bind to and degrade the host teichoic acids to expose the peptidoglycan layer
152 for degradation by other proteins of the baseplate.
153

154 **Hub proteins facilitate penetration of the tail tube through the cell wall and membrane**

155 The three hub proteins form a ring, extending the tail channel into the phi812 baseplate (Fig. 1D and
156 2). Phi812 hub protein can be divided into channel-forming domains I to IV and clamp and cleaver
157 domains (SFig. 7B). The channel-forming domains I and III have beta-barrel folds and are positioned

158 next to each other so that the head-proximal interface formed by the trimer of hub proteins has
159 pseudo-sixfold symmetry for binding the hexamer of tube initiator proteins (Fig. 2, SFig. 7B). In
160 contrast, the channel-forming domains II and IV of the hub protein, positioned below domains I and
161 III respectively, are structurally distinct and form interfaces for binding the trimer of central spike
162 proteins to the inside of the hub channel (Fig. 2, SFig. 7B). The channel-forming domains I-IV are
163 structurally similar to those of the gp27 of phage T4, for which the domain naming convention was
164 established[36] (Table S2). Homologs of the channel-forming domains can also be identified among
165 phages with long non-contractile tails (Tal proteins)[20,38] and CISs (Vgrg-like proteins)[19,39,40] (Table S2).
166 The cleaver domain of the hub protein, the structure of which was determined using NMR
167 (Fig. 4D, SFig. 7B, Table S3), has the characteristic fold of the cysteine- and histidine-dependent
168 amido-hydrolase/peptidase (CHAP)[41], and contains the conserved catalytic triad
169 Cys699-His759-Glu777[42] (Fig. 4D). Accordingly, zymogram analysis demonstrated that a recombinant
170 cleaver domain degrades *S. aureus* cell walls (hence the name cleaver) (SFig. 8), which agrees with
171 previous functional studies of hub protein homologs from the related phage K[43,44]. The clamp domain
172 of the hub protein is formed by ten short α-helices that connect the central spike protein to weld
173 proteins (Fig. 1C, D, and 4E, SFig. 7B and 9). The clamp domain is structurally similar to pore-forming
174 saposin-like proteins, which employ positively charged residues to interact with the negatively
175 charged surfaces of lipid membranes (Table S2)[45,46]. Since the clamp domain of the phi812 hub
176 protein contains a long positively charged patch of residues, as the saposin-like proteins do (Fig. 4E),
177 we speculate that it may bind the *S. aureus* membrane to facilitate its penetration by a tail tube. In
178 addition to gp27 of T4 featuring a lysozyme domain, more hub proteins equipped with enzymatic
179 domains have been reported recently[8,27]. Therefore, we propose that the hub proteins of phi812 and
180 related phages enable genome delivery by degrading peptidoglycan to facilitate penetration of the
181 tail tube through the cell wall.
182

183 **Tail tube initiator, weld, assembly, and tail sheath initiator proteins complete the baseplate core**

184 Three weld proteins bind to the central spike, hub, and three inner tripod proteins, connecting them
185 together. Six assembly and six tail sheath initiator proteins surround the hub and tail tube initiator
186 proteins to complete the structure of the baseplate core (Fig. 1C, D, and 2). The tube initiator and
187 sheath initiator proteins are organized with sixfold symmetry, whereas the central spike, weld, hub,
188 and assembly proteins are organized with threefold symmetry that determines the overall
189 organization of the baseplate in its native conformation (Fig. 1C, D, and 2).
190 The weld protein of phi812 can be divided into the N-terminal lid and C-terminal clip
191 domains, which are connected by a 14-residue-long linker (SFig. 7D). The lid domain interacts with an
192 inner tripod and serves as a lid covering the peptidase site of the cleaver domain of the hub protein
193 (SFig. 9). Therefore, releasing the weld protein from the baseplate upon host cell binding exposes the
194 active site of the cleaver domain of hub protein to hydrolyze cell wall peptidoglycan. The clip domain
195 of the weld protein, located closer to the tail axis, binds the weld protein to the central spike protein.
196 The clip domain has the CHAP protein fold similar to that of the cleaver domain of the hub protein
197 (Fig. 4F). However, the clip domain lacks the conserved catalytic residues Cys-His-Glu required for the
198 peptidoglycan cleavage[42] (Fig. 4F). Thus, the clip domain is likely enzymatically inactive, but may have
199 retained peptidoglycan-binding ability, similar to the RipD protein from *M. tuberculosis*[47]. There is no
200 homolog of the weld protein in the baseplate of the related phage A511[18,48]. The weld protein may

be unnecessary for A511 because of the differences in the cell wall composition between *Staphylococcus* and *Listeria*[49].

The assembly protein of phi812 is formed by a compact bundle of nine α-helices. The assembly protein interacts with the wedge protein and C-terminal handle of the tail tube initiator protein (Fig. 1D and 2). There are proteins with a compact globular structure and in the equivalent position in the baseplates of pyocin R2 and phages Pam3, E217, A-1 and Milano (Table S2), indicating the structural role of these proteins in baseplate cores[4,6,8,9,22].

The hexamer of tail tube initiator proteins binds to the trimer of hub proteins and, on the other side, to a hexamer of tail tube proteins (Fig. 1C and 2). The tail tube initiator protein can be divided into the N-terminal β-barrel domain and the C-terminal α-helical handle, which stretches along the hub protein and reaches the assembly protein in the baseplate core (SFig. 7C). The tail tube initiator proteins from pyocin R2 and phages E217 and Pam3 contain extensions similar to the C-terminal handle of the phi812 tail tube initiator protein, suggesting an evolutionary link between phage and pyocin baseplates[2,20].

The tail sheath initiator protein of phi812 is composed of the LysM and handshake domains (SFig. 7E). The handshake domain, containing two β-strands, interacts with the N- and C-termini of tail sheath proteins from the first tail sheath disc and the C-terminus of tail sheath protein from the second tail sheath disc to form a five-stranded β-sheet (SFig. 7E and 10C). The same mechanism that connects the tail sheath initiator proteins to tail sheath proteins connects successive discs of the tail sheath proteins. Therefore, the interactions of the N- and C-termini of the tail sheath proteins with the handshake domains can initiate tail sheath assembly. Proteins containing domains with structures similar to the handshake domain are integral to the baseplates of most CISs and phages with contractile tails (Table S2)[19,39,50].

Wedge modules attach baseplate arms to the baseplate core

Wedge modules are structural components of phage baseplates, which enable the attachment of peripheral baseplate proteins to the baseplate core[3,51]. Here, we show that the wedge module of phi812 is formed by two wedge proteins with different conformations, A and B, and the N-terminal 176 residues of arm scaffold protein (Fig. 1C and 2, SFig. 4B and 6, Table S2, SMovie 1). Wedge protein can be divided into N-terminal α-helices, wing, trifurcation, and dimerization domains, and the part of the arm scaffold protein belonging to the wedge module can be divided into N-terminal α-helices and a trifurcation domain (SFig. 4B and 7F, G). Individual parts of the phi812 wedge module are structurally conserved and can be found in the baseplate of phage T4[3]. The N-terminal helices and trifurcation domains mediate contacts between the proteins forming the wedge module (Fig. 2, SFig. 6A). The wing domain of wedge protein A binds to the hub and central spike proteins. In contrast, the wing domain of wedge protein B binds to the first disc of tail sheath proteins (Fig. 1B-D and 2). The six wedge modules form an iris around the baseplate core (Fig. 1D, SFig. 6A), as described in phage T4[3]. Dimerization domains of wedge proteins mediate interactions between neighboring wedge modules (SFig. 6A). Even though the neighboring wedge modules differ in their conformations due to the overall threefold symmetry of the native baseplate, the contacts between the dimerization domains are similar (SFig. 6A-C, F).

Baseplate arms provide attachment sites for receptor-binding proteins

The baseplate arm of phi812 includes the arm scaffold protein, which forms the backbone of the arm, and arm segment proteins that reinforce the arm structure (Fig. 3A-C). Each of the baseplate arms of phi812 is formed by linker AB, bulge, linker BC, elbow, linker Z, and connector domains of the arm scaffold protein that are held in place by three dimers of the arm segment proteins, named arm segments A, B, and C (Fig. 3D, E, SFig. 4B). We employed X-ray crystallography to determine the structure of the arm segment protein (Fig. 3D, Table S4), and AlphaFold2[52] to predict the structures of the arm scaffold protein domains, which could not be built into the cryo-EM map due to its limited resolution (Fig. 3E, SFig. 4). Each arm segment protein is composed of an N-terminal α-helix followed by a three-layered β-sandwich (Fig. 3D). The overall structure of arm segment protein is similar to those of gp8 from phage T4 and gp105 from phage A511[18,53] (Table S2). When looking along the baseplate arm towards the baseplate core, arm segments B and C are rotated clockwise 125° and 250°, respectively, relative to arm segment A (Fig. 3B). The C-terminal beta-strands of neighboring subunits of arm segments A and B are separated by 10.2 Å (Fig. 3F). As was proposed previously[18], the gap is probably filled by a β-strand formed by the linker AB of the arm scaffold protein, creating a continuous, seven-stranded β-sheet. The linker BC of the arm scaffold protein probably connects the β-sheets of arm segments B and C using the same strand insertion mechanism.

The arm scaffold protein provides attachment sites for two trimers of tripod proteins, one trimer of RBP1, and one trimer of RBP2. The trifurcation domain of the arm scaffold protein contains 28-residue-long docking loop 1, which forms the binding site for the inner tripod complex (Fig. 3A, E, SFig. 4B). Similarly, the bulge domain of the arm scaffold protein contains 40-residue-long docking loop 2, which enables attachment of the outer tripod complex (Fig 3A, SFig. 4B). The elbow domain with a double β-sandwich fold and C-terminal connector domain with a β-sandwich fold of the arm scaffold protein are located at the distal end of the baseplate arm, and probably provide attachment sites for RBP1 and RBP2, respectively (Fig. 1B and 3A, SFig. 4B).

Receptor-binding proteins

High-avidity interactions between the baseplate and the cell wall mediate the attachment of phi812 to *S. aureus*. Major components of the *S. aureus* cell wall are peptidoglycan formed by N-acetylglucosamine, N-acetylmuramic acid, and oligopeptides and teichoic acids built from polymerized ribitol-phosphate decorated with acetylglucosamine (GlcNAc)[49,54]. It has been shown that the backbone of the wall teichoic acid is essential for the adhesion of phi812 and related phages K, phiSA012, and phiMR003 to the host cell, whereas GlcNAc serves as a co-receptor[55–58]. The baseplate of phi812 contains 36 tripod proteins and 18 of each of RBP1 and RBP2 (Fig. 1A, B and 5). As discussed above, additional putative receptor-binding domains are within the hub and central spike proteins.

The structure of a trimer of tripod proteins in a native baseplate resembles a three-sided pyramid (Fig. 5A). The tripod protein can be divided into the spine, flap, fiber, base, fin, leg, anchor, and hook domains (Fig. 5C). The spine domain is positioned next to the axis of the pyramid, the flap and fiber domains form the edge, and the base domain forms the base of the pyramid. The fin, leg, anchor, and hook domains are located at the faces (Fig. 5A, C). The flap domain contains an insertion loop, three of which enable the binding of the tripod complex to the arm scaffold protein (Fig. 5C,

SFig. 4B and 11A, B). The interaction between the inner tripod complex and the arm scaffold protein is well resolved in the reconstruction of a contracted baseplate (SFig. 11A-C). A three-pointed star-shaped crevice, formed by the spine domains of the tripod proteins, binds the docking loop 1 of the trifurcation domain of the arm scaffold protein (SFig. 11A-C). Since the bulge domain of the arm scaffold protein contains a docking loop 2 with hydrophobic residues in equivalent positions to those of the docking loop 1 of the trifurcation domain (SFig. 11D), the inner and outer tripod complexes are likely attached to the arm scaffold protein using similar interactions. The docking loop 2 of the bulge domain, which binds the outer tripod complex, is twelve residues longer than the docking loop 1 of the trifurcation domain (SFig. 11D). The extra residues of the docking loop 2 probably enable the ~170° rotation of the outer tripod complexes during the baseplate transformation induced by the binding of phi812 to a host cell. The base and fin domains of tripod proteins have ten-stranded β-sandwich folds of carbohydrate-binding module families 16 and 61[59,60] (Fig. 5C, Table S2), indicating that they may bind glycans from the *S. aureus* cell wall. The leg domain includes fifteen β-strands, eight forming a β-sandwich that is structurally similar to lectin-like protein Cwp84 from *C. difficile*[61] (Fig. 5C, Table S2), suggesting another possible receptor-binding site. The anchor domain with a β-sandwich fold is followed by the hook domain with sequence similarity to LysM proteins, indicating it may bind peptidoglycan[62] (Fig. 5C, SFig. 12, Table S2). In the native phi812 baseplate, RBP1 and RBP2 are positioned between baseplate arms (Fig. 1A, B). As the cryo-EM reconstruction of the native baseplate did not resolve RBP1 and RBP2 to sufficient resolutions to enable structure determination, we employed AlphaFold2[52] prediction to obtain the structures of RBP1 and RBP2 (Fig. 5D, E, SFig. 2A).

The predicted structure of the RBP1 trimer has the shape of a triangular bipyramid with a height of 186 Å and a width of the base of 102 Å (Fig. 5D). RBP1 consists of an antenna domain, three tower domains, and a tip domain, all positioned along the symmetry axis of the trimer, and a wing domain protruding laterally from the second tower domain (Fig. 5D, Table S2). The tower domains are structurally similar to each other and contain characteristic six-stranded β-sheets (Fig. 5D). The antenna domain mediates the binding of RBP1 to the end of the baseplate arm, probably to the connector domain of the arm scaffold protein (Fig. 1B). The tower domain III and tip domain of RBP1 interact with the tower domain 1 of the RBP2 attached to the baseplate arm located clockwise when looking at the baseplate in the direction of the phage head (Fig. 1A, B).

The RBP2 trimer has the shape of a cylinder with a length of 207 Å and a diameter of 56 Å (Fig. 5E). Like RBP1, RBP2 is formed of an antenna domain, three tower domains, and the tip domain (Fig. 5E, Table S2). The antenna domain enables the binding of RBP2 to the end of the baseplate arm near arm segment C (Fig. 1B). The tip domain of RBP2 is in contact with a wedge module (SFig. 5).

Re-arrangement of RBP and tripod complexes is required for baseplate binding to a cell wall

Tailed phages use receptor-binding proteins from their baseplates to attach to host cells[1]. For phages with contractile tails, the receptor binding is accompanied by reorganization of the baseplates, which may include conformational changes to individual proteins[1,3,17]. It has been proposed that the reorganization starts at the baseplate periphery, propagates to the inner baseplate, and triggers the contraction of the tail sheath[2,3]. Upon binding to the *S. aureus* cell wall, the phi812 baseplate broadens to a diameter of 713 Å, and its thickness decreases to 344 Å (Fig. 6, SFig 1, 2D-F and 3, Table S1). The conformational change transforms the baseplate to sixfold symmetry, with all six baseplate arms protruding at 83° relative to the tail axis (Fig. 6B, C, SMovie 3). Comparing the

329 structures of the native and contracted baseplates of phi812 enabled us to propose the sequence of
330 steps of the baseplate rearrangement. Reorganization of the baseplate is probably initiated by the
331 rotation of RBP1 and RBP2 trimers so that they can bind to the cell wall (Fig. 1B and 6B, C, SMovie 3).
332 RBP1 trimers are not resolved in the reconstruction of the baseplate from phages with contracted
333 tails, likely due to the flexible connection of RBP1 to arm scaffold protein (Fig. 6A-C, SFig. 2D). RBP2
334 trimers swing away from the baseplate core to orient themselves parallel with the tail axis and their
335 tip domains facing away from the phage head (Fig. 1B, 6B, C, SMovie 3). Subsequently, the outer
336 tripod complexes can rotate 170° to point their receptor-binding domains away from the phage head
337 (Fig. 1B, 6B, C, SMovie 3). The inner tripod complexes tilt by 6° and rotate 28° to assume positions
338 with their axes parallel to the tail axis (Fig. 1B, 6B, C).

339 The tripod complexes not only rotate, but also undergo complex conformational changes
340 (Fig. 5C, SMovie 4): (i) The second and third spine helices move towards the first spine helix by 10
341 and 16 Å, respectively. (ii) The fiber domain moves 13 Å towards the flap domain and rotates 20°
342 counterclockwise around the tripod symmetry axis when looking from the bottom of the tripod. (iii)
343 The base domain shifts 24 Å along the third spine helix while rotating 174° around an axis
344 perpendicular to the tripod symmetry axis. (iv) The fin domain moves 56 Å to protrude laterally from
345 the tripod. (v) The three leg domains detach from the flap domains and move 88 Å to interact with
346 each other under the base domains. (vi) The anchor and hook domains were not resolved in the
347 cryo-EM reconstruction of the contracted baseplate; however, contracted phage particles attached to
348 the cell wall contain density under the tripod complexes, suggesting that the anchor and hook
349 domains stretch along the tripod axis toward the cell wall (Fig. 5C, SFig. 13). Similar density under the
350 tripod complexes was observed in micrographs of contracted phage A511 attached to *Listeria* cells,
351 and in the baseplate reconstructions of the spontaneously contracted phi812[17] and A511[18]. Because
352 of their positioning after the tripod conformational change, we speculate that the hook loops of
353 phi812 and related phages could bind the host cell wall.

354 The tripod proteins' conformational changes are required to form inter-tripod and
355 tripod-RBP2 interactions in phages with contracted tails (Fig. 6B, C, SFig. 14). In particular, the
356 rotation and translation of the base domain expose an interface to which a fiber domain of the
357 neighboring tripod complex binds through an area of 1,900 $Å^2$ (SFig. 14). Each inner tripod complex
358 also connects to an outer tripod complex attached to the same baseplate arm, and one fiber domain
359 of each outer tripod complex interacts with tower domains 1 and 2 of RBP2 (Fig. 6A-C). The contacts
360 mediated by the fiber domains stabilize the baseplate structure in phages with contracted tails.

361 The formation of interactions among the inner trimers of tripod proteins causes the upper
362 and lower baseplate arms to shift 11 and 15 Å away from the tail axis, respectively, relative to their
363 positions in the native baseplate (Fig. 1B, 6B, C). Simultaneously, all six baseplate arms are shifted to
364 radiate from the tail axis at 83°, establishing the sixfold symmetry of the baseplate (Fig. 6A, B). Less
365 extensive conformational changes were described for the receptor-binding proteins of other
366 phages[4,63,64]. Overall, the recognition and adhesion of phi812 to the host cell is accompanied by
367 re-orientation of the RBP1, RBP2, and conformational changes of tripod complexes, affecting the
368 positions of the six arms of the contracted baseplate.

369

370 **Conformational changes to the baseplate core prompt tail sheath contraction**

371 The structure of baseplate core is affected by the re-arrangements of receptor-binding proteins and
372 baseplate arms, which in turn triggers the contraction of the tail sheath. The arm scaffold proteins

covalently link baseplate arms of phi812 to the wedge modules (Fig. 2 and 3A-C, SMovie 2). Therefore, the changes in the position and orientation of baseplate arms cause the iris-like structure formed by the wedge modules to expand in radius from 52 to 61 Å (SFig. 6A, D). The expansion of the iris is enabled by the movement of the dimerization and trifurcation domains relative to each other (SFig. 6B, C and E, SMovie 5). In contrast, the interactions between the dimerization domains of wedge proteins remain the same as in the native baseplate (SFig. 6F). A similar expansion was described for gp6 and gp7 during the transition of the T4 baseplate from its native to contracted state[3]. The expansion of the radius of the hexamer of tail sheath initiator proteins of phi812, which probably occurs together with that of the wedge iris, is enabled by the partial unfolding of the linker helices between LysM and handshake domains (SFig. 10A, B, D, and E, SMovie 5). The unfolding of the linker enables the tail sheath initiator proteins to maintain the same contacts within the hexamer and with wedge modules as in the native baseplate (SFig. 10G, H). The handshake domain of the tail sheath initiator protein inclines 17° (SFig. 10B, E) and, together with the wedge iris expansion, triggers the contraction of the tail sheath, as discussed below.

The native tail of phi812 can bend

Contractile tails of phages differ in their length and mechanical properties. Whereas the ~100-nm-long tails of *Straboviridae* phages, represented by T4, are rigid[65]. A flexible contractile tail has been observed only in phage Milano[9] (genus *Schmittlotzvirus*, unclassified family) with ~125-nm-long tail, and in the *Herelleviridae* phages phi812 and A511 with ~200-nm-long tails that can bend up to 90°[17,18]. The flexibility of the longer tails was speculated to be an adaptation to withstand mechanical forces without breaking[66]. Here, we determined the structure of the native phi812 tail to a resolution of 4.2 Å (Fig. 6D, SFig. 1, 2G and 3, Table S1). Both tail tube and tail sheath proteins are arranged as six-start helices with a rise of 39.2 Å and twist of 21.2° (Fig. 6D). The tail tube protein of phi812 has an eight-stranded β-barrel fold with a protruding stacking loop, characteristic for tail tube proteins of long-tailed phages and CISs[66] (SFig. 7I, Table S2). The inner surface of the phi812 tail tube is negatively charged to facilitate the passage of the phage DNA during ejection (SFig. 15A). The β-barrel domain of tube protein subunit contains a short loop between the β-strands 6 and 7, lack of which was suggested to allow bending of tail tube of phage Milano[9]. Since the loop is present in phi812 tail tube protein, bending of the phi812 tail is likely allowed by a different mechanism. The sheath protein of phi812 can be divided into domains I-IV, according to the convention established for the tail sheath protein (gp18) of phage T4[2] (SFig. 7H). In a native tail, the domains I and II of phi812 tail sheath proteins interact with tail tube proteins and mediate substantial contacts between tail sheath proteins. Domains III and IV are positioned successively next to domain II at the tail surface (SFig. 15B). The two-stranded β-sheet of domain I is augmented by accepting the N- and C-termini of tail sheath proteins from a disc positioned closer to the phage head (SFig. 15C). By mediating the handshake interactions, the domain I interconnects tail sheath proteins from successive discs. These interactions are conserved in tail sheath structures of numerous phages and CISs[3–9,22–26,67,68]. The domain II of the tail sheath protein is formed by six β-strands surrounded by eight α-helices, whereas domains III and IV each contain a beta-sandwich flanked by an alpha-helix (SFig. 7H). The domain III contacts domain IV of the tail sheath protein from the disc located closer to the baseplate (SFig. 15D). Additionally, domain IV interacts with domain II of the neighboring tail sheath protein from the same disc (SFig. 15D). The domain IV of the T4 gp18 is not involved in inter-subunit contacts[69]; however, the bulkier domain III of the T4 tail sheath protein

(168 residues) interacts with another tail sheath protein from the disc closer to the phage head[69]. We speculate that interactions of domains III and IV of the phi812 tail sheath proteins allow a spring-like movement of the subunits relative to each other, which enables phi812 tail bending.

Contraction of the tail sheath

In phages with contractile tails and CISs, the rearrangement of the baseplate induced by binding to a target cell wall triggers the contraction of the tail sheath, which transforms from the native state to a lower energy contracted state[70]. The released energy of the tail sheath contraction is used to drive the tail tube through the host cell wall[4,8,17,18,22]. Upon contraction, the tail sheath of phi812 broadens from 219 to 276 Å in diameter, which is coupled to a change in the rise and twist of the six-start helix formed by the tail sheath proteins to 18.8 Å and 30.6°, respectively (Fig. 6E, SFig. 1, 2H, I and 3, Table S1). The successive discs of the contracted tail sheath are brought closer to each other due to the tilting of domain I 47° compared to its native conformation while maintaining the inter-subunit handshake interactions among domains I from successive discs (Fig. 6F, SFig. 15E, F). The buried surface area of intersubunit contacts per tail sheath monomer increases from ~5,500 $Å^2$ in the native tail sheath to ~9,500 $Å^2$ in the contracted tail sheath. The enlarged contacts stabilize the straight structure of the contracted tail sheath, which is less flexible than the native one[17]. During contraction, the individual domains of the tail sheath protein of phi812, unlike those of T4 and some CISs[26,69,71], move relative to each other, which enables the formation of the more extensive contacts between the subunits (SFig. 15G).

It has been shown for phages T4 and A511 and R-type diffocin that the contraction of the tail sheath is gradual and occurs as a wave along the tail axis[18,27,70,72]. In agreement with the previous *in vitro* observations, we captured particles of phi812 with a partially contracted tail sheath attached to the *S. aureus* cell wall (SFig. 13). Furthermore, the cryo-EM reconstructions of baseplate-proximal parts of the tails in the native and contracted state provide structures of discrete intermediates of contraction (SFig. 2B, E, and 16, SMovie 5). The first three baseplate-proximal tail sheath discs of the native phi812 tail sheath differ in conformation from those in the central part of the native tail sheath (SFig. 16A, B). The deviation occurs gradually, with the first tail sheath disc being the most affected (SFig. 16B). Similar deviations of baseplate-proximal tail sheath proteins were observed in the R2 pyocin and T6SS[22,73]. The first three sheath discs of phi812 have their organization shifted toward that of the contracted tail sheath, which may reduce the activation energy required to initiate the tail sheath contraction[74].

In the contracted state of phi812, the structures of the first six baseplate-proximal tail sheath discs deviate from those from the central part of the contracted tail sheath (SFig. 16C, D). Similar to the native tail sheath, the first contracted sheath disc is the most affected and the sixth one the least affected (SFig. 16D). The first two baseplate-proximal sheath discs have the rise increased by 5.5 Å relative to the tail sheath disc from the center of the contracted tail sheath (SFig. 16D). The absence of a twist difference may be due to the more extensive contacts between consecutive tail sheath discs than in the native tail, which is probably incompatible with deviations in the angle of the helical twist. Interactions with the sheath initiator and wedge module proteins likely cause the altered structure of the baseplate-proximal tail sheath discs and directly couple the conformational changes of baseplate proteins with the sheath contraction.

460 **Changes in the baseplate structure required for cell wall penetration**

461 Phages with contractile tails infecting Gram-positive bacteria employ enzymes that degrade teichoic
462 acid and peptidoglycan to facilitate tail tube penetration through the cell wall[54,75]. Phage phi812
463 probably uses the petal domain of the central spike protein to cleave teichoic acid (Fig. 4B, C and 7A,
464 B); however, the central spike protein needs to be released from the tail channel to enable the
465 genome ejection. We speculate that the conformational change to inner tripod trimers, which
466 disrupts their interaction with weld proteins, triggers the release of the weld and central spike
467 proteins from the baseplate (Fig. 7B, C, SFig. 9). Dissociation of the weld and central spike proteins is
468 required to enable the cleaver domains of the hub protein to interact with and degrade the cell wall
469 peptidoglycan (Fig. 4D, E, SFig. 9D). This indicates that the weld and central spike proteins of phi812
470 are released before the cell wall penetration by the tail tube (Fig. 7D). In contrast, the central spike
471 proteins of phages T4 and E217, which infect Gram-negative bacteria, are released from baseplates
472 after puncturing the host outer membrane[4,76,77].
473 As the phi812 tail sheath contracts, the tip of the tail tube is pushed through the degraded
474 teichoic acid and peptidoglycan layers while rotating about its axis by 475° (Fig. 7D). The rotation of
475 the hub proteins at the tip of the tail tube can enhance their peptidoglycan degradation activity by
476 bringing them into contact with more substrate. Once the peptidoglycan layer is breached, the clamp
477 domains of the hub proteins can interact with the *S. aureus* cytoplasmic membrane. It was shown
478 that after the penetration of the outer membrane and peptidoglycan layer, gp27 from T4 (a homolog
479 of the hub protein from phi812) remains associated with the tip of the tail tube and probably
480 interacts with ejected tape measure protein to form a pore through the inner membrane of *E. coli*[78].
481 However, the tail tube of phi812 penetrates 10-30 nm into the *S. aureus* cytoplasm, depending on
482 the thickness of the cell wall, which varies between 50-70 nm[17] (Fig. 7E). Therefore, unlike in T4, the
483 hub proteins of phi812 are probably not required to form a pore in the *S. aureus* membrane, and
484 their role in genome delivery may be limited to facilitation of the penetration of the cell wall and
485 cytoplasmic membrane by the tail tube tip.
486
487 **Conclusions**

488 In this study, we employed a combination of cryo-EM, X-ray crystallography, NMR, and structure
489 prediction methods to elucidate the intricate mechanisms employed by phage phi812 to penetrate
490 the *S. aureus* cell wall in preparation for transferring its genetic material into the host cytoplasm.
491 While most of the previously structurally characterized phages with contractile tails target
492 Gram-negative bacteria, our focus has been on phi812 attacking *S. aureus*, a representative of
493 Gram-positive bacteria, which are comparatively less explored. We show that the baseplate of the
494 phage phi812 comprises a core, wedge modules, and baseplate arms that carry RBP1, RBP2, and
495 tripod complexes (Fig. 1A-C, SMovies 1, 2). Upon binding to the *S. aureus* cell wall, the baseplate
496 symmetry transitions from threefold to sixfold, which is enabled by a series of conformational
497 changes that propagate from the baseplate periphery to the core (Fig 6A, B, SMovies 3, 4). These
498 changes encompass a reorientation of receptor-binding proteins and conformational changes to
499 tripod complexes to enable host cell surface binding (Fig. 7A, B, SMovie 3). The baseplate contains
500 thirty six tripod proteins with one hundred eighty potential binding sites, eighteen receptor-binding
501 proteins 1 with thirty six potential binding sites, and eighteen receptor-binding proteins 2 with

eighteen potential binding sites. During the attachment, the central spike protein degrades teichoic acid (Fig. 7A, B). Conformational changes to the tripod complexes trigger the release of the central spike and weld proteins from the baseplate, which enables the hub proteins to cleave peptidoglycan (Fig. 7C, D) and facilitate penetration of the tail tube through the cell membrane (Fig. 7D, E). Changes in the baseplate arms' positions relayed through wedge modules to the hexamer of tail sheath initiator proteins cause an expansion of its diameter, triggering a tail sheath contraction (Fig. 7C-E, SMovie 5). The baseplate-proximal tail sheath discs of the native phage particle have an altered structure, which may lower the energy barrier required to initiate the tail sheath contraction. The tail sheath shortens from 200 to 96 nm upon contraction[17], pushing the tail tube's tip 10-30 nm into the cytoplasm, depending on the local thickness of the *S. aureus* cell wall. The molecular characterization of the phi812 baseplate structure and the mechanism of cell wall binding open up the possibility of a rational design of phi812 to target specific strains of *S. aureus*.

Figures

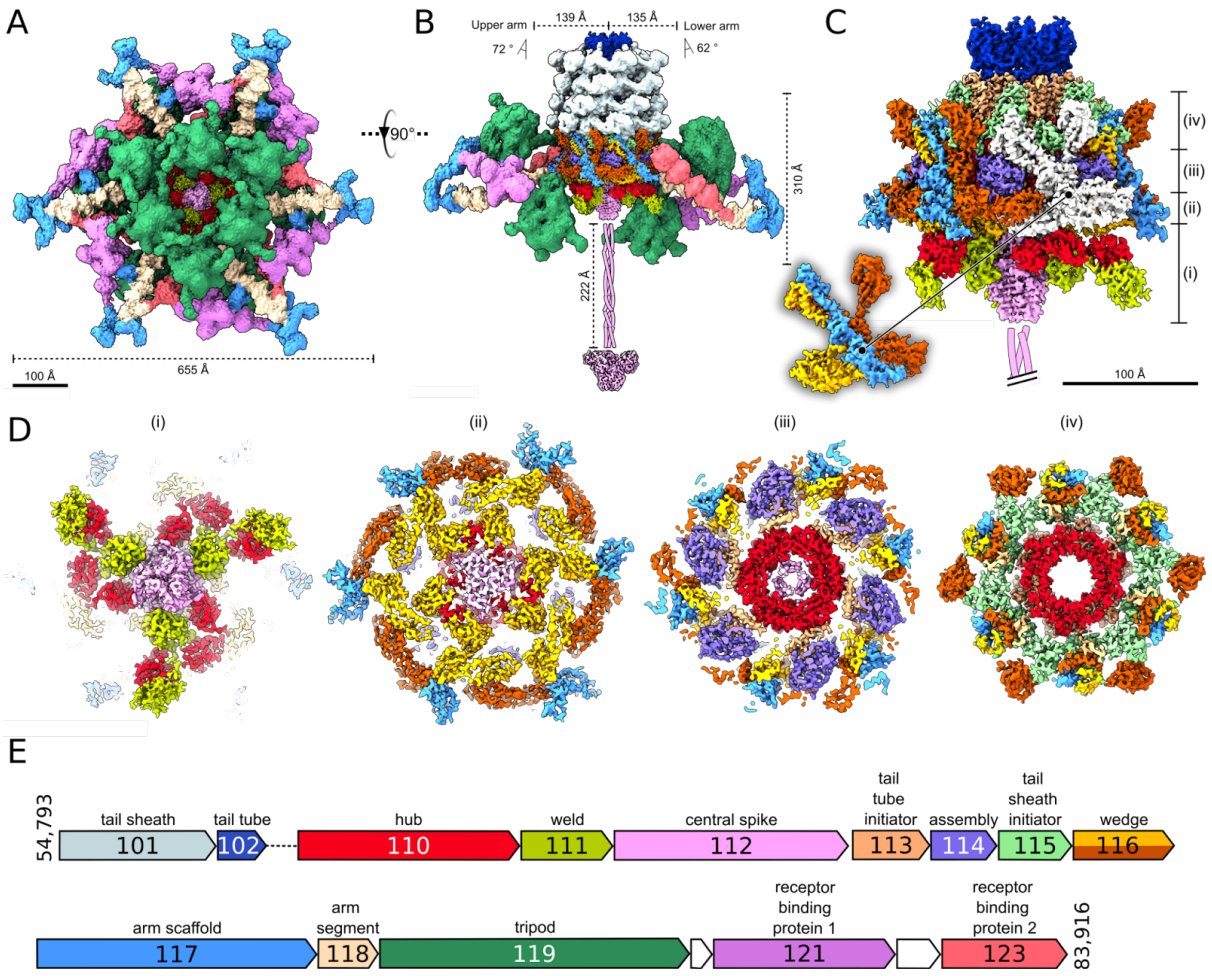

Fig. 1. Structure of native phi812 baseplate. (A-D) The surface representation of the composite cryo-EM map of the phi812 baseplate is viewed along (A, D) and perpendicular to (B, C) the tail axis. Protein components of the baseplate are colored according to the scheme depicted in panel E. The part of the central spike protein protruding from the baseplate is not shown in (A). **(B)** Side view of phi812 baseplate. Only two opposing baseplate arms are shown to display the structure of the baseplate core. The height of the baseplate, angles of baseplate arms relative to the tail axis, distances of baseplate arms from the tail axis, and length of the coiled-coil domain of the central spike protein are indicated. **(C)** A complex of tail tube disc, baseplate core proteins, and wedge modules. A single wedge module shown in white in the complex is displayed at the bottom left to highlight interactions among the arm scaffold and two wedge proteins. The positions of sections shown in panel (D) are indicated on the right. **(D)** Sections through the baseplate core proteins and wedge modules at positions indicated in panel C. **(E)** Scheme of part of the phi812 genome encoding tail and baseplate genes.

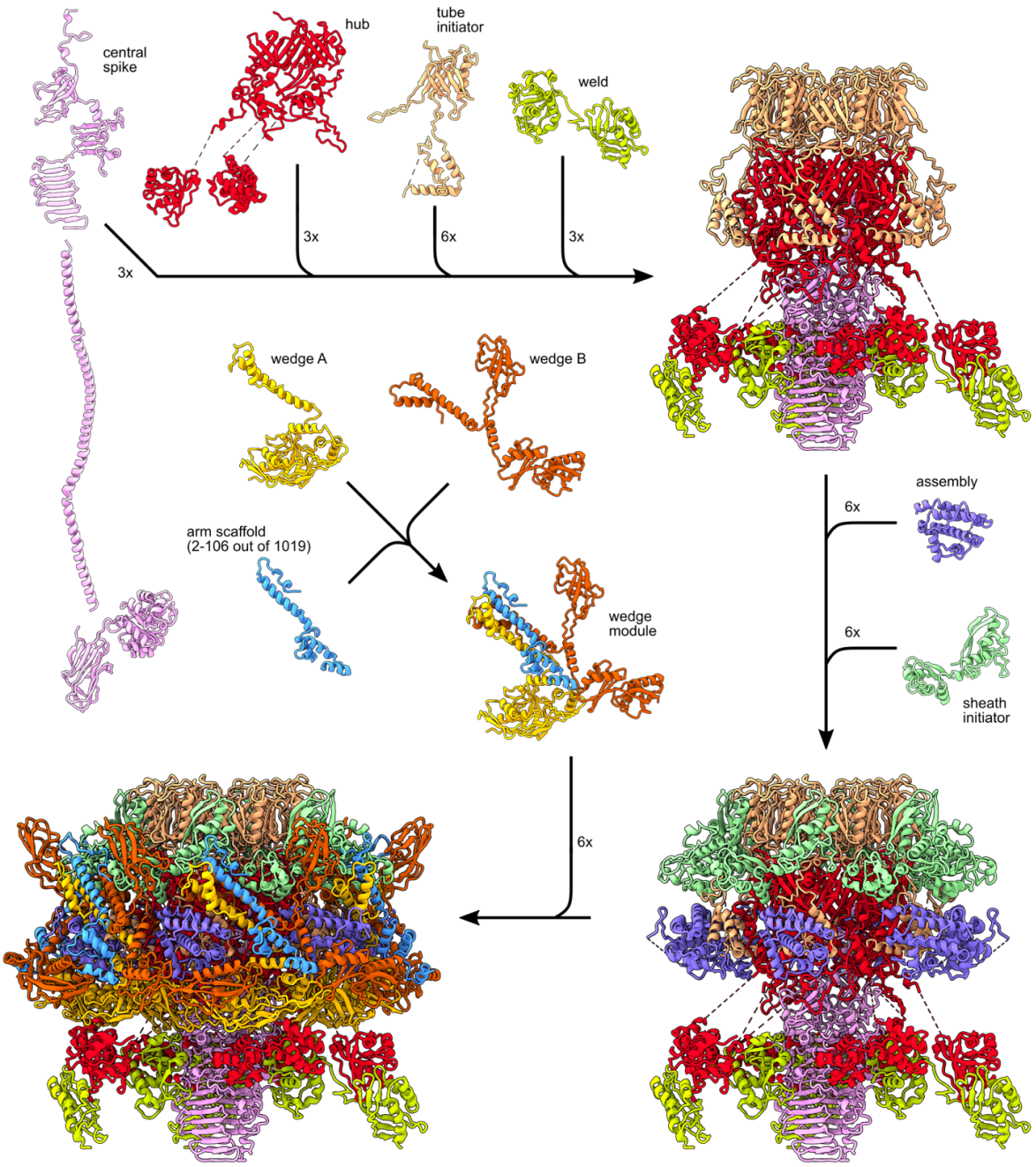

Fig. 2. Components of phi812 baseplate core and wedge modules. The baseplate core and wedge module proteins are shown in cartoon representation and colored according to Fig. 1E. Protein names and the numbers of subunits of each protein forming the baseplate core and wedge modules are indicated.

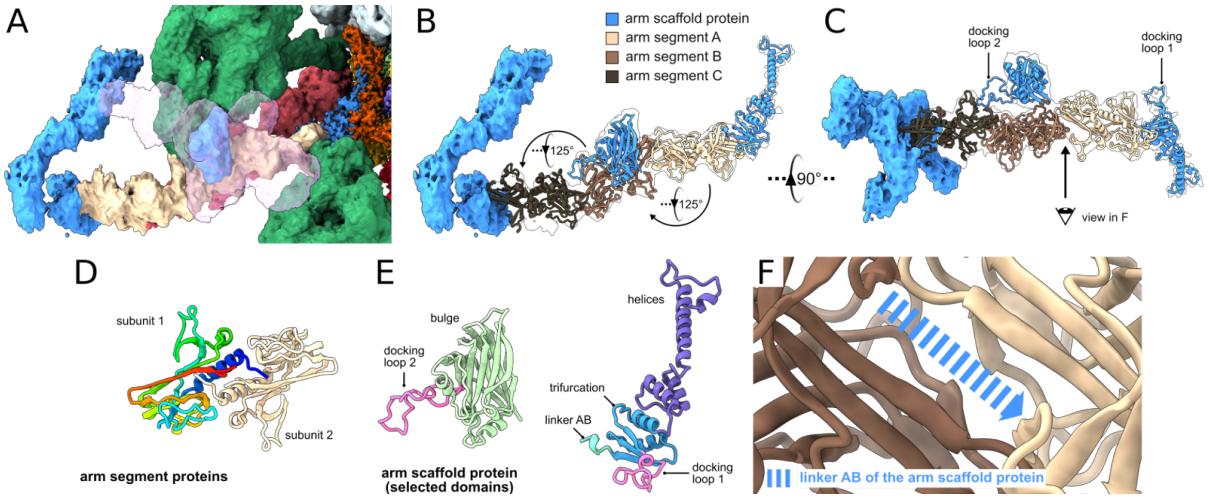

Fig. 3. Structure of phi812 baseplate arm. (A) Surface representation of cryo-EM reconstruction of phi812 baseplate in native conformation, showing one baseplate arm with attached receptor-binding proteins. The densities corresponding to the baseplate arm, wedge module, and tail sheath proteins were segmented and are shown in color according to Fig. 1E, except for RBP1, which is shown as a semi-transparent surface. **(B, C)** The N-terminal helices, trifurcation domain, bulge domain and docking loops 1 and 2 of the arm scaffold protein and arm segment proteins are shown in cartoon representation. The corresponding cryo-EM map of a native baseplate is depicted as a semi-transparent white surface with a black outline. Cryo-EM density of the distal part of the baseplate arm, probably corresponding to elbow and connector domains, is shown as a blue surface. The arm scaffold protein and arm segment protein dimers A, B, and C are colored according to the legend. **(C)** Same as panel B, but rotated 90°. Docking loops 1 and 2 of the arm scaffold protein that attach the inner and outer tripod protein trimers, respectively, are indicated. The direction in which the interface between arm segment protein dimers A and B is viewed in panel F is indicated. **(D)** Cartoon representation of the arm segment protein dimer, with one of the subunits rainbow colored from the N-terminus in blue to the C-terminus in red. **(E)** Cartoon representations of selected domains of the arm scaffold protein predicted by AlphaFold2. Orientation of the domains corresponds to those shown in cartoon in panel B. **(F)** Cartoon representation of the interface between the C-terminal β-strands of arm segment dimer A (beige) and dimer B (light brown) shown in cartoon representation. The dashed blue arrow indicates a speculative position of a beta-strand formed by the linker AB of the arm scaffold protein.

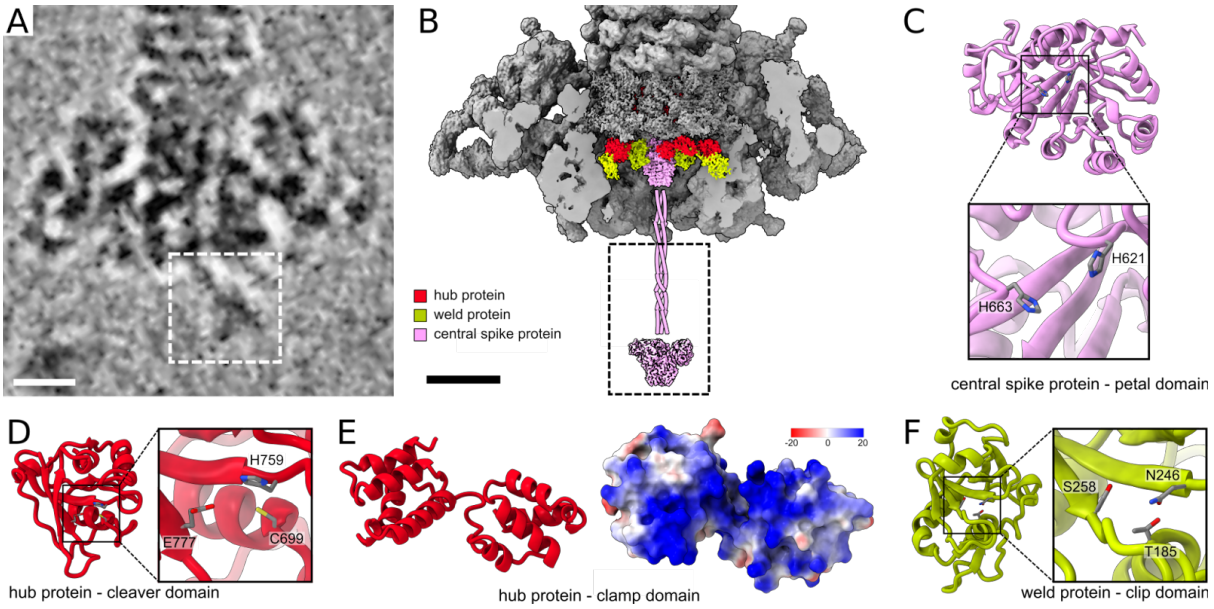

Fig. 4. Central spike, hub, and weld proteins. (A) Cryo-electron micrograph of the phi812 baseplate. The white dashed rectangle contains the coiled-coil, knob, and petal domains of the trimer of central spike proteins. Scale bar 100 Å. **(B)** The surface representation of the cryo-EM reconstruction of the native phi812 baseplate is colored in gray except for central spike, hub, and weld proteins. The front part of the baseplate has been removed. Scale bar 100 Å. **(C)** Cartoon representation of the petal domain of the central spike protein. Side chains of residues forming a putative hydrolytic site are shown in stick representation. The inset shows details of the putative hydrolytic site. **(D)** The cleaver domain of the hub protein is shown in cartoon representation with side chains of residues forming a putative hydrolytic site shown in stick representation. **(E)** Clamp domain of the hub protein shown in cartoon representation (left) and the molecular surface colored according to Coulombic electrostatic potential (right) in the range from -20 to 20 kcal/(mol·*e*) at 298 K. **(F)** Cartoon representation of the clip domain of the weld protein with side chains of residues forming a putative receptor-binding site shown in stick representation.

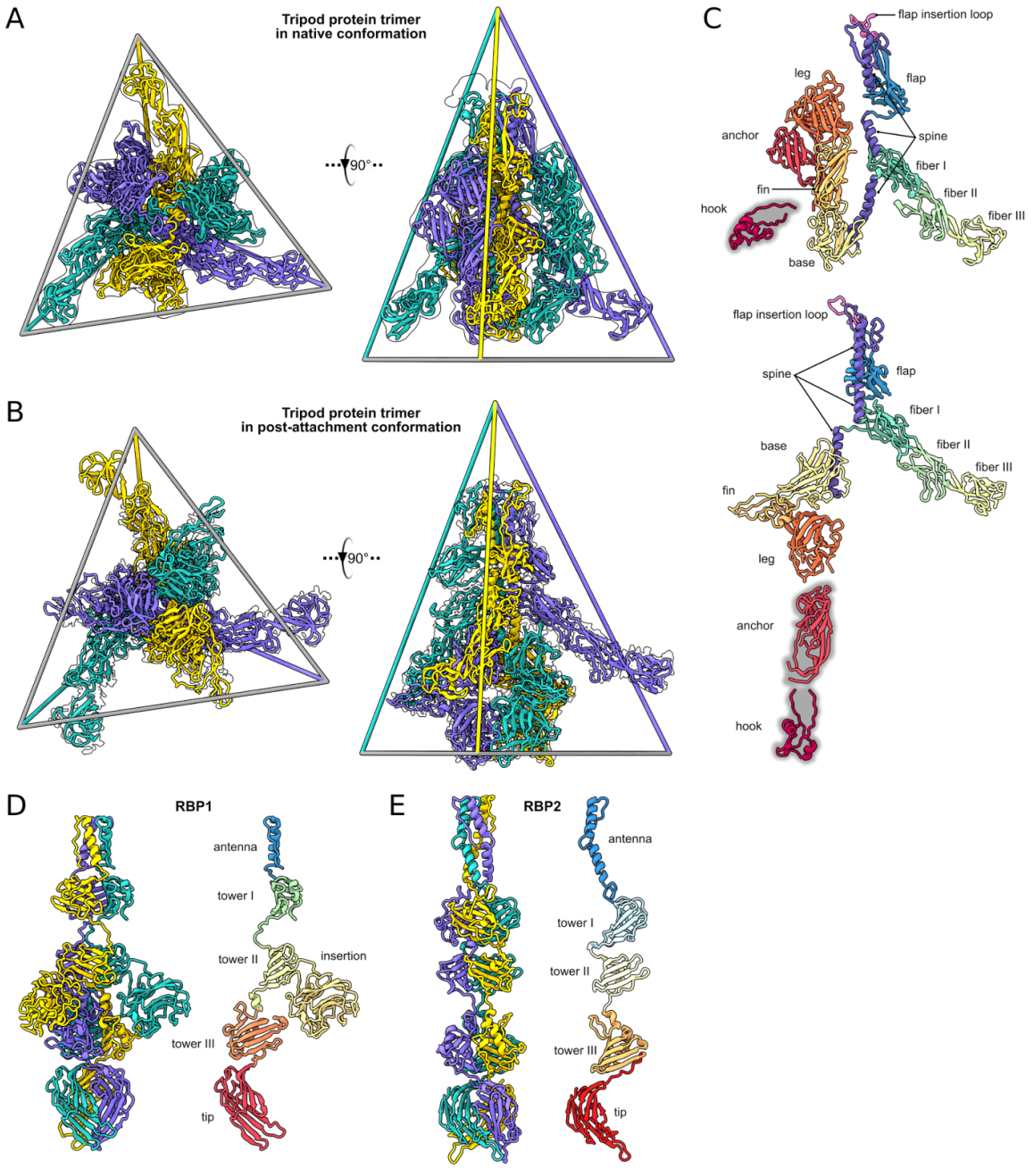

Fig. 5. Tripod and receptor-binding proteins. (A) Cartoon representation of an AlphaFold2-predicted structure of a trimer of tripod proteins in native conformation. Subunits are distinguished by color. The structure is fitted into the cryo-EM density of a native baseplate, which is shown as a black outline. Only the domains of tripod proteins for which the density was resolved are shown. **(B)** The trimer structure of tripod proteins in the post-attachment conformation was determined using cryo-EM reconstruction of the contracted phi812 baseplate. Only the domains of tripod proteins for which the density was resolved are shown. Triangular cages in (A) and (B) highlight the shape of the tripod protein complexes. **(C)** Cartoon representations of tripod proteins in native (top) and post-attachment (bottom) phi812 baseplates. The structures are colored according to domain. Domains with gray backgrounds were not resolved in the corresponding reconstructions, and their positions are speculative. **(D, E)** RBP1 (D) and RBP2 (E) structures predicted using AlphaFold2 are shown in cartoon representations colored according to subunit (left). A single subunit of each protein colored according to domain is shown (right).

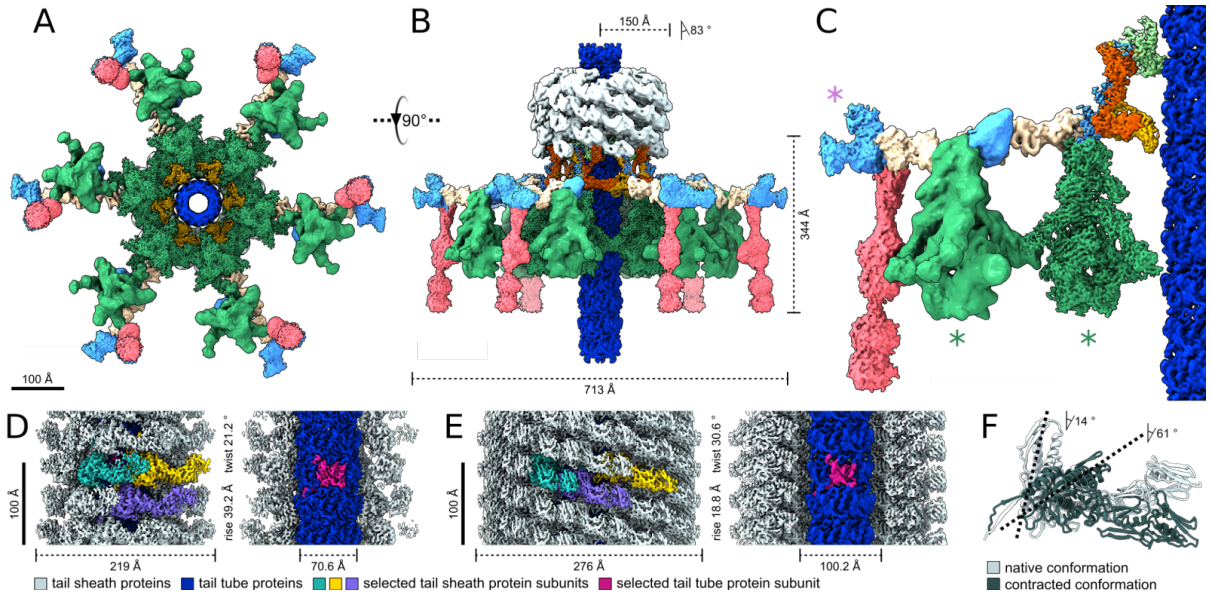

Fig. 6. Structure of baseplate from phi812 particle with contracted tail and conformational changes of phi812 tail sheath induced by contraction. (A-B) The surface representation of the composite cryo-EM map of the phi812 baseplate is viewed along (A) and perpendicular to (B, C) the tail axis. Protein components are colored according to the scheme depicted in Fig. 1E. (B) The width and height of the baseplate are indicated at the bottom and on the right, respectively. The angle of the baseplate arm and its distance from the tail axis are displayed at the top. **(C)** One arm of phi812 baseplate. A pink asterisk indicates the putative attachment site of RBP1, which was not resolved in the reconstruction. Green asterisks indicate volumes occupied by anchor and hook domains of the tripod complexes, which were not resolved in the reconstruction. **(D, E)** Surface representation of cryo-EM map of the native (D) and contracted (E) tail of phi812. For each panel, complete maps are shown on the left, and maps with the front half of the tail sheath removed on the right. Protein components are colored according to the legend below the panel. **(F)** Comparison of the structures of tail sheath proteins in native and contracted conformations. The structures are shown in cartoon representation, and their domains II were superimposed. Angles of the long axes of domain I relative to the tail axis are indicated for each conformation.

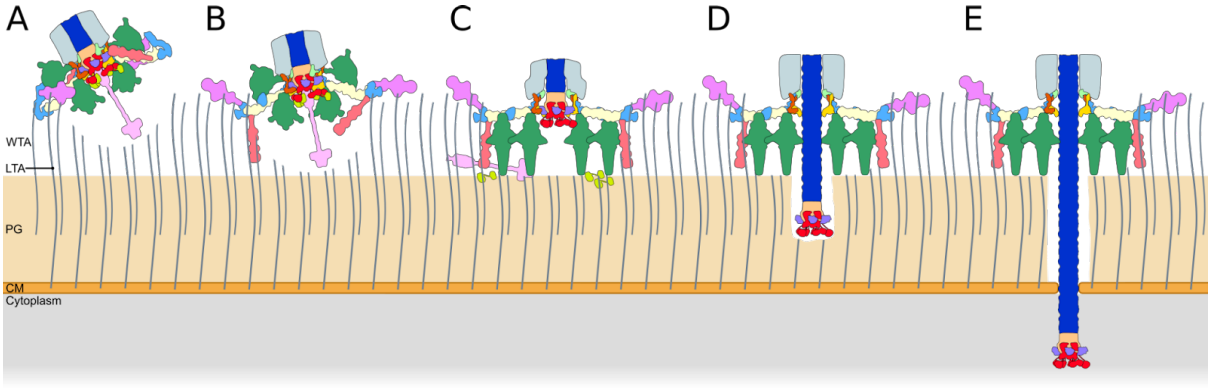

Fig. 7. Scheme of phi812 cell adhesion and penetration. (A) Upon contact of the phage phi812 baseplate with the cell wall of *S. aureus*, trimers of RBP1 bind to teichoic acid. The petal domains of the central spike proteins cleave teichoic acid below the baseplate. **(B)** Trimers of RBP2 rotate and bind to teichoic acid. **(C)** Tripod complexes undergo a conformational change and anchor the baseplate to the cell wall. Central spike and weld proteins detach from the baseplate. The diameter of the iris formed by wedge modules increases, leading to a conformational change to tail sheath initiator proteins and baseplate-proximal sheath discs. The remaining baseplate core proteins detach from the sheath initiator and wedge module proteins. **(D)** As the contraction of the sheath discs propagates towards the phage head, the tail tube with tail tube initiator, hub, and assembly proteins at its tip is driven through the cell wall. The cleaver domain of the hub protein degrades the peptidoglycan. **(E)** The tail tube penetrates the cytoplasmic membrane, and its tip reaches the cytoplasm. However, whether the baseplate core proteins remain associated with the tip of the tail tube during the membrane penetration remains unknown. WTA - wall teichoic acid; LTA - lipoteichoic acid; PG - peptidoglycan; CM - cytoplasmic membrane.

Supplementary figures

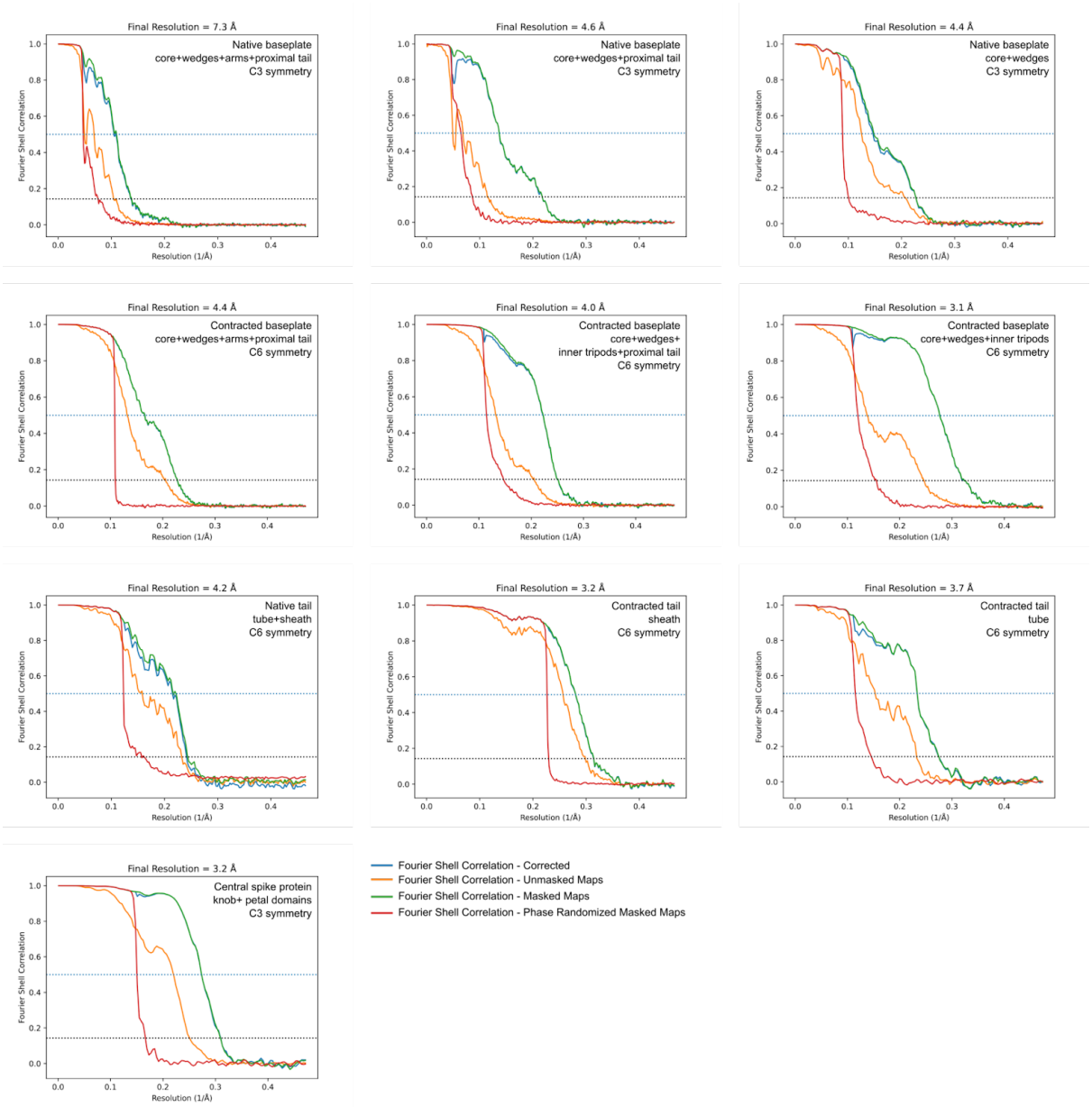

SFig. 1. FSC curves of cryo-EM reconstructions. Each panel shows a comparison of Fourier shell correlation curves color-coded according to the legend. The FSC threshold levels are indicated by a blue dotted line (threshold 0.5) and a black dotted line (threshold 0.143).

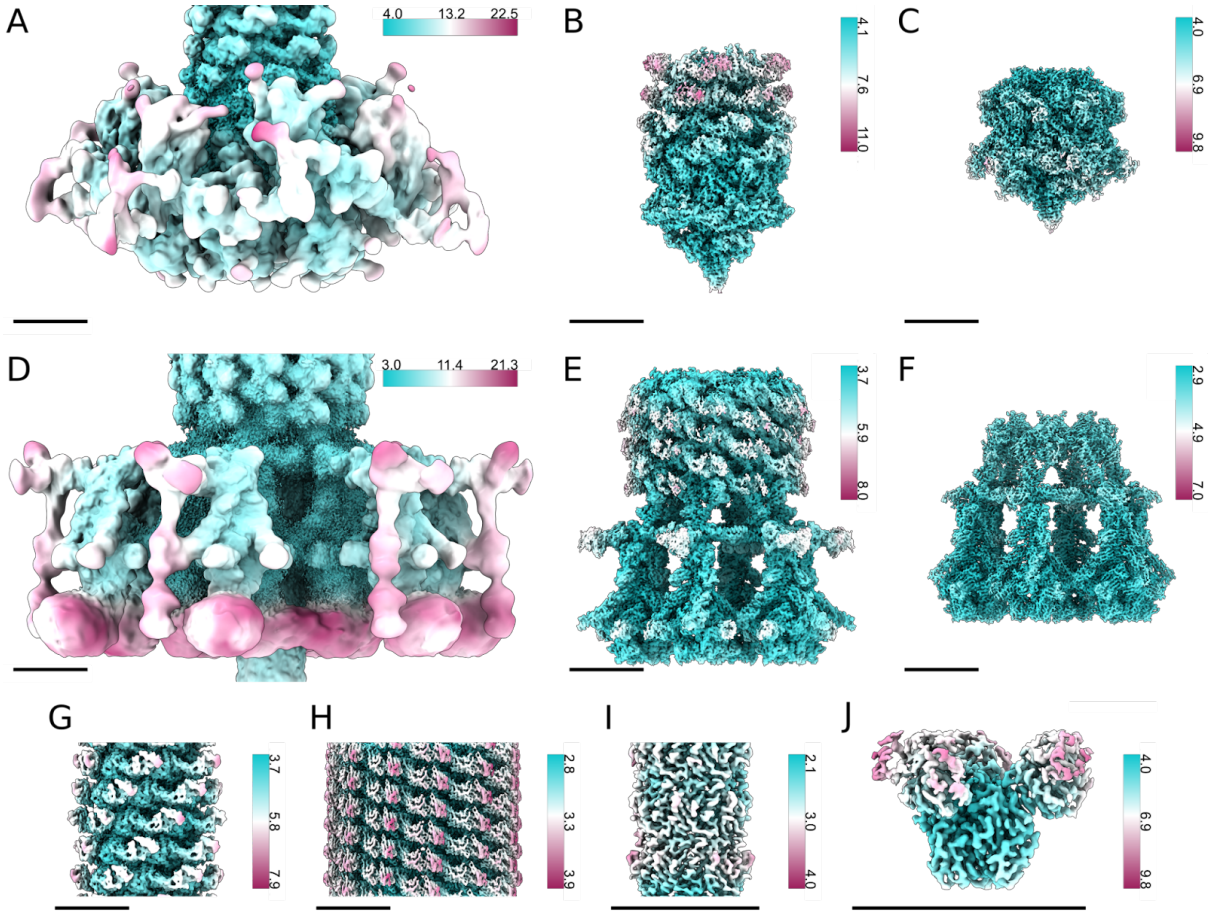

SFig. 2. Local resolution maps of cryo-EM reconstructions. (A-J) Surface representations of cryo-EM reconstructions colored according to the local resolution in Å. Scalebars = 100 Å. **(A)** Native baseplate. **(B)** Core, wedge modules, and three tail sheath discs of the native baseplate. **(C)** Core and wedge modules of the native baseplate. **(D)** Contracted baseplate. **(E)** Tail sheath initiator proteins, wedge modules, inner tripod proteins, arm segments A, and six tail sheath discs of the contracted baseplate. **(F)** Sheath initiator proteins, wedge modules, and inner tripod proteins of the contracted baseplate. **(G)** Native tail sheath and tail tube. **(H)** Contracted tail sheath. **(I)** Tail tube from the contracted tail. **(J)** Knob and petal domains of the central spike protein.

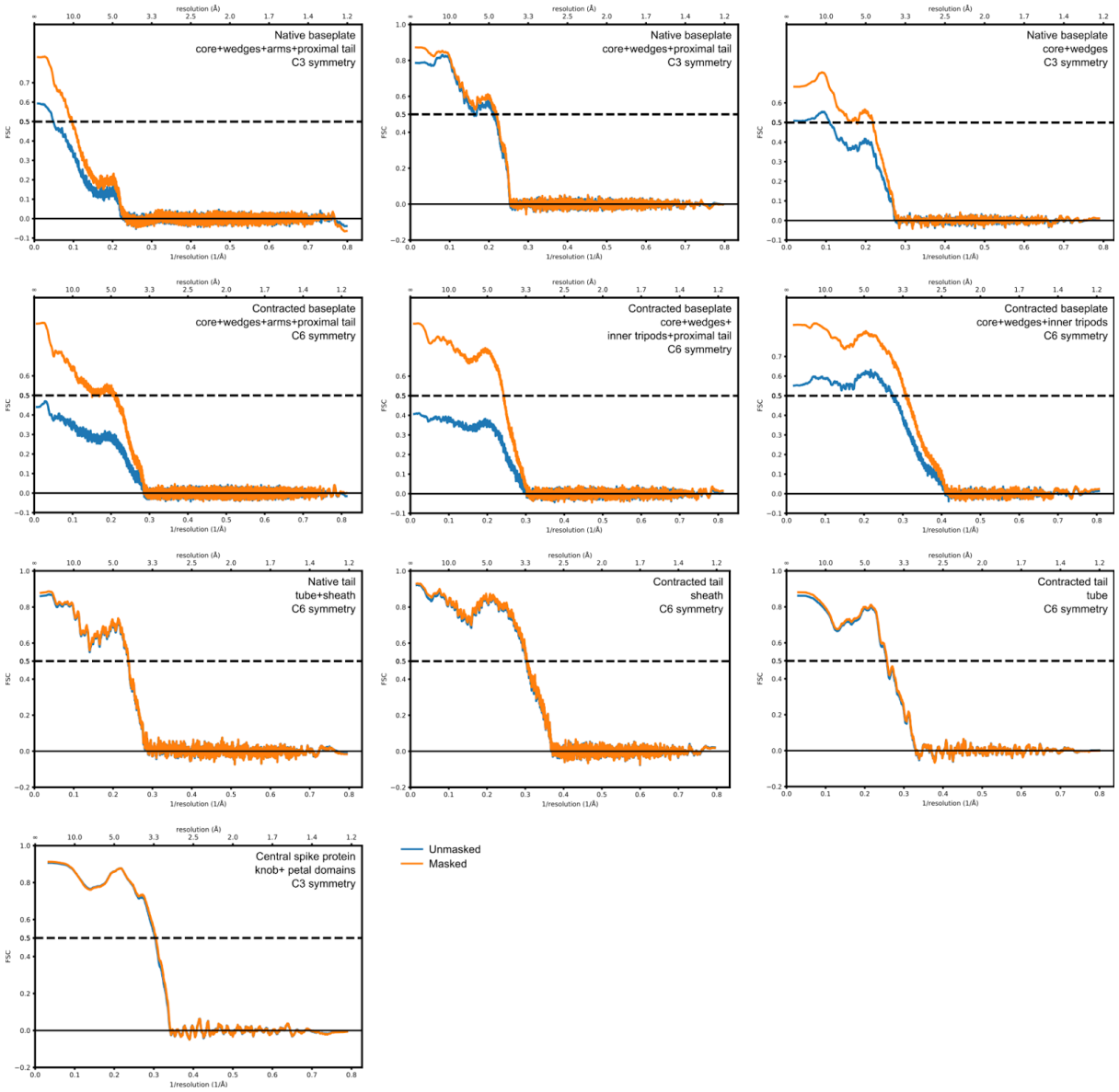

SFig. 3. Map to model FSC curves of cryo-EM reconstructions. Each panel shows a comparison of Fourier shell correlation curves color-coded according to the legend. The differences between the masked and unmasked FSC curves in some of the structures are due to the presence of unmodelled densities. The FSC threshold levels are indicated by a black dotted line (threshold 0.5) and a black line (threshold 0).

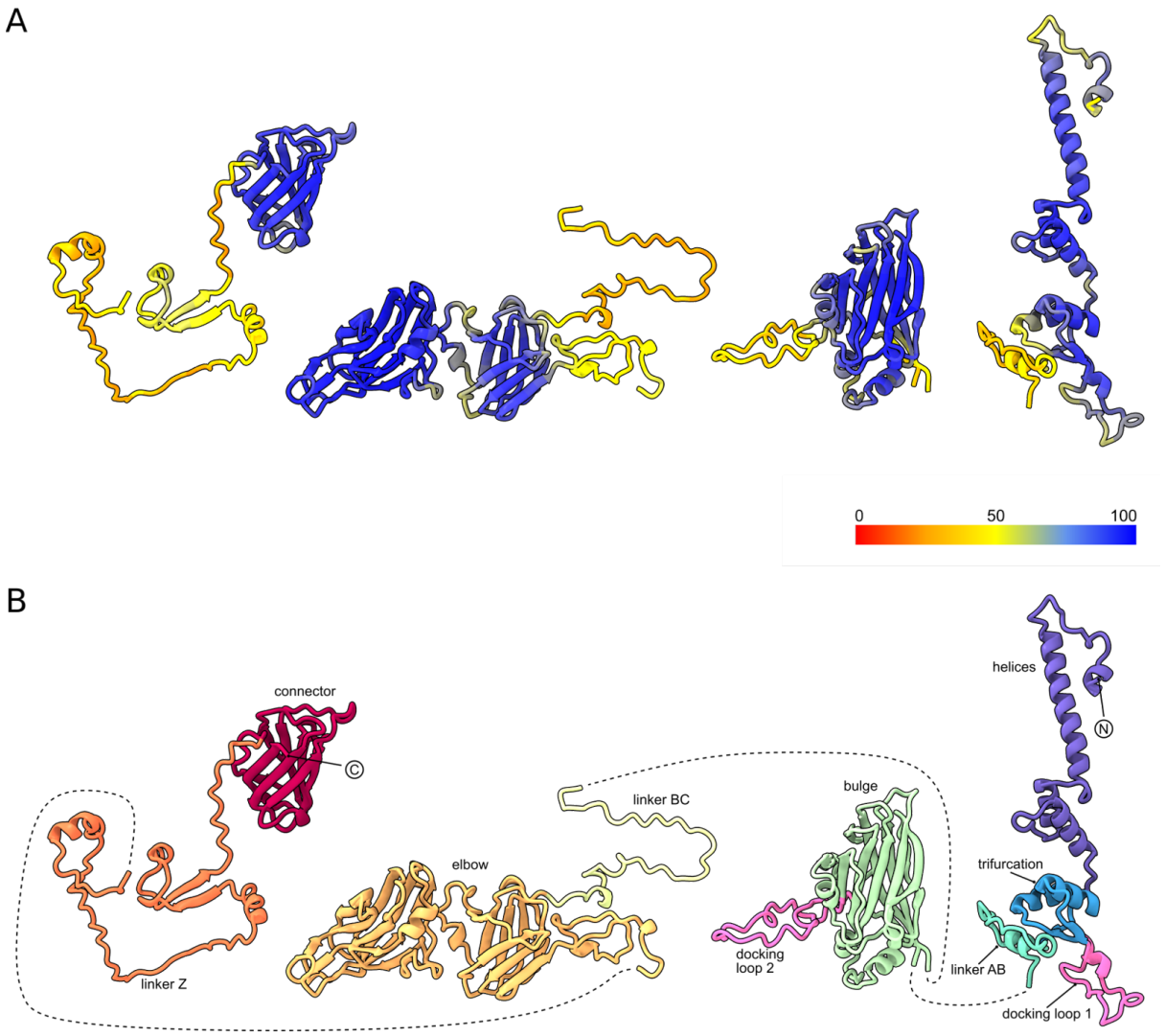

SFig. 4. Arm scaffold protein. (A,B) AlphaFold2-predicted structure of the arm scaffold protein shown in cartoon representation and colored according to pLDDT score[52] (A) and domain composition (B). The structure was divided into several parts for better visualization. In (B), domain names and chain termini are indicated. Dashed lines indicate connections among domains.

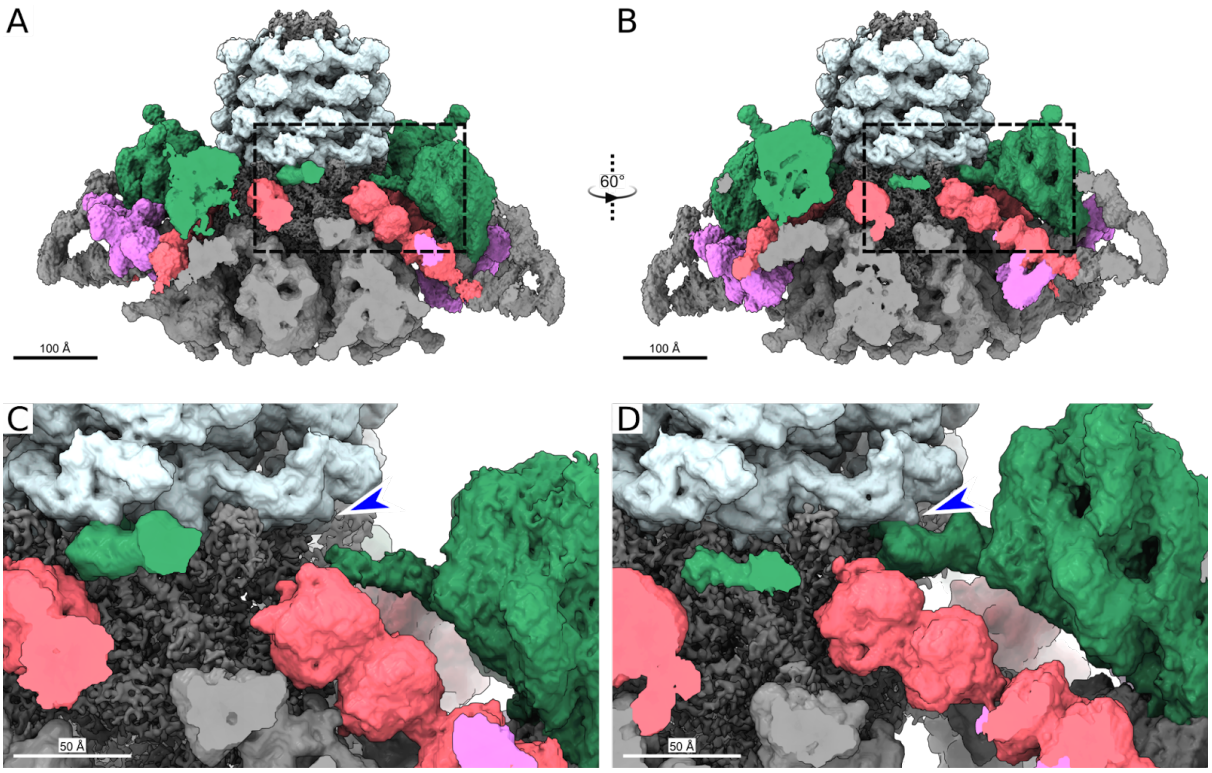

SFig. 5. Comparison of interactions of tripod proteins, RBP1, and RBP2 attached to upper and lower baseplate arms with baseplate core and tail sheath. Surface representation of a composite cryo-EM map of the native phi812 baseplate. All proteins are colored gray except the tail sheath proteins in white, tripod proteins in green, RBP1 in magenta, and RBP2 in firebrick red. The front part of the baseplate density has been removed to display the interactions of the receptor binding proteins from the lower **(A, C)** and upper **(B, D)** baseplate arm with the baseplate core and tail sheath. Rectangles in A and B indicate close views, as shown in C and D. Blue arrowheads point to the sites where the interactions of the lower (C) and upper (D) baseplate arms with the tail sheath differ.

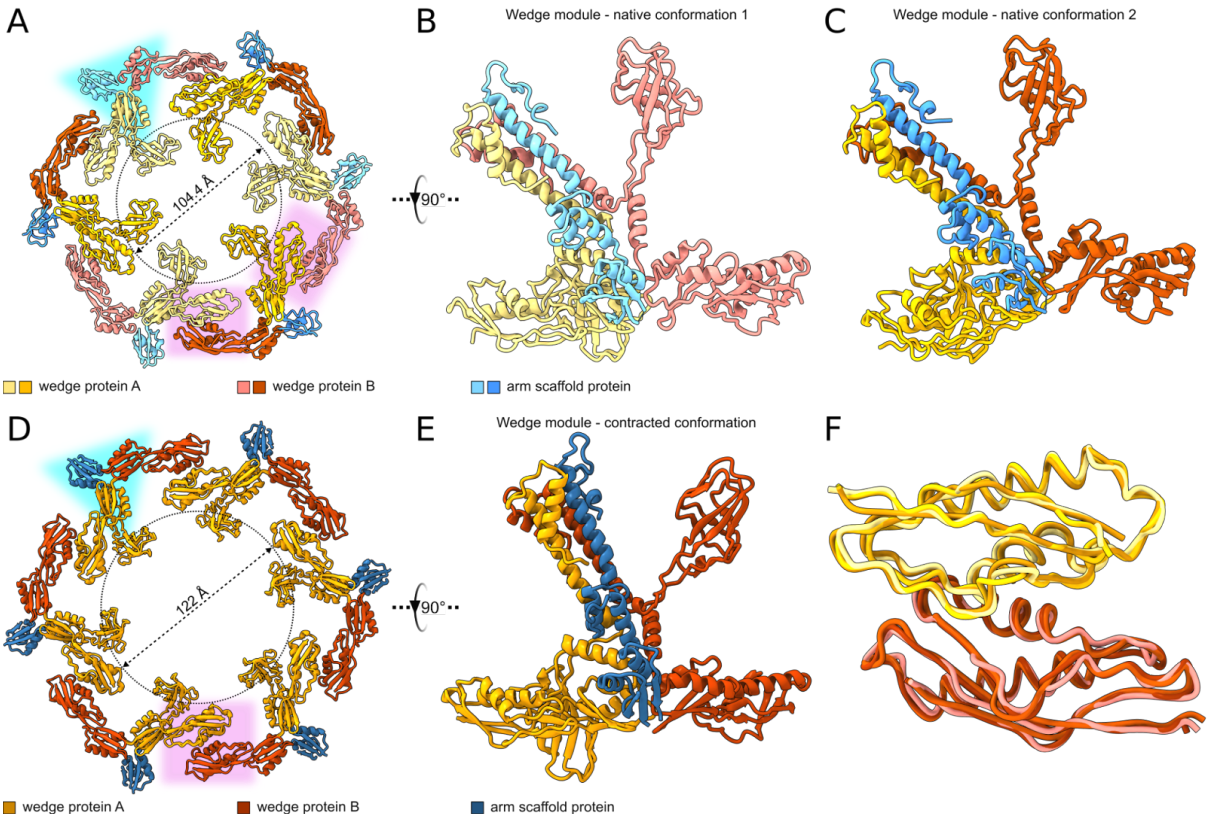

SFig. 6. Expansion of iris formed by wedge modules upon phi812 tail contraction. (A-C) Cartoon representation of wedge modules from the native phi812 baseplate is colored according to the legend at the bottom. (A) Six wedge modules forming the iris are viewed along the tail axis towards the phage head. Three wedge modules that enable the attachment of lower arms are shown in lighter colors, and the three wedge modules that enable the attachment of upper arms are shown in darker colors. The hetero-trimer interface formed by trifurcation domains is highlighted in cyan. Two conformationally different dimer interactions of dimerization domains are highlighted with magenta backgrounds. (B, C) A single wedge module in conformation 1 (B) and 2 (C). **(D-F)** Wedge modules from the contracted baseplate of phi812 are shown in cartoon representation and colored according to the legend at the bottom. (D) Six wedge modules forming the iris structure viewed along the tail axis towards the phage head. The hetero-trimer interface formed by trifurcation domains is highlighted in cyan. The interfaces of dimerization domains are highlighted in magenta. A dotted circle indicates the inner diameter of the wedge iris. (E) A single wedge module from the contracted baseplate. (F) Superimposition of three pairs of dimerization domains, which are highlighted in magenta in panels A and D.

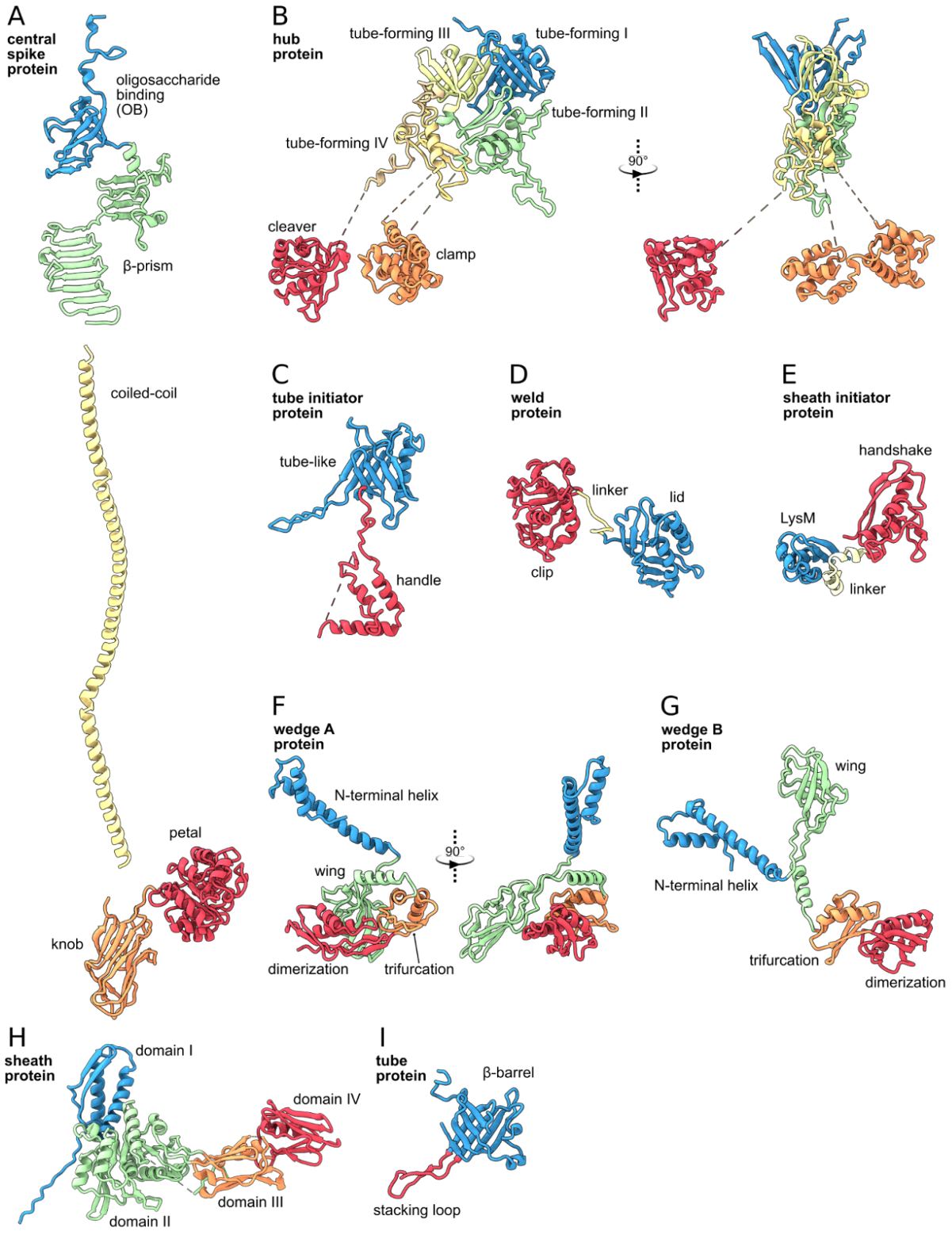

SFig. 7. Domain organization of proteins forming baseplate core, wedge modules, and tail of phi812. (A-I) The proteins are shown in cartoon representation and colored according to domains and functional elements. The names of proteins are in bold.

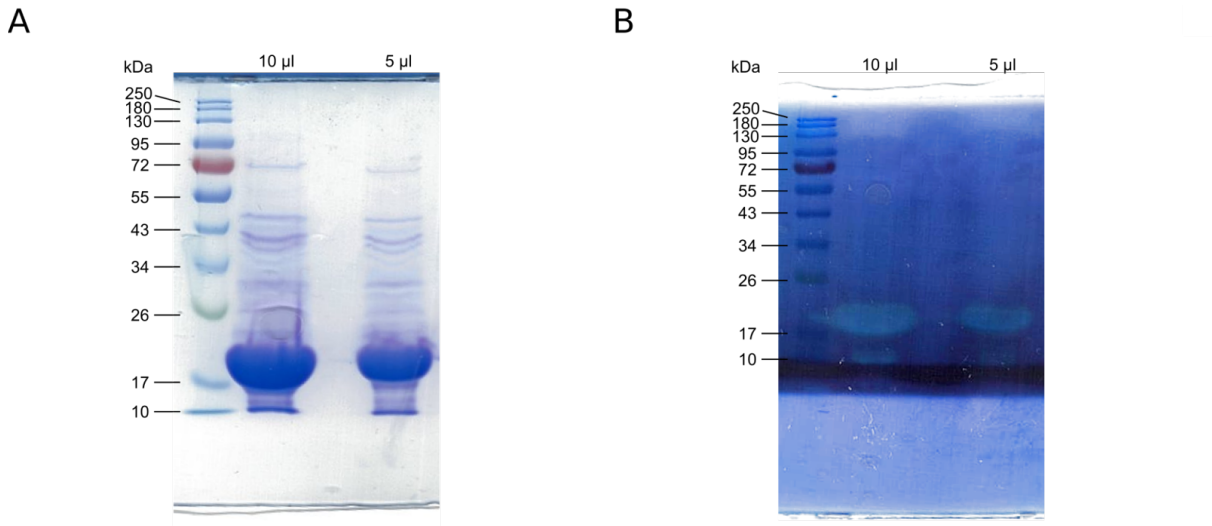

SFig. 8. SDS-PAGE and zymogram analysis of cleaver domain of hub protein. Scan of an SDS-PAGE gel **(A)** and zymogram **(B)** of recombinantly expressed cleaver domain of the hub protein after Histrap purification. As indicated, ten and five µl of the purified protein sample concentrated to 10 mg/µl were loaded.

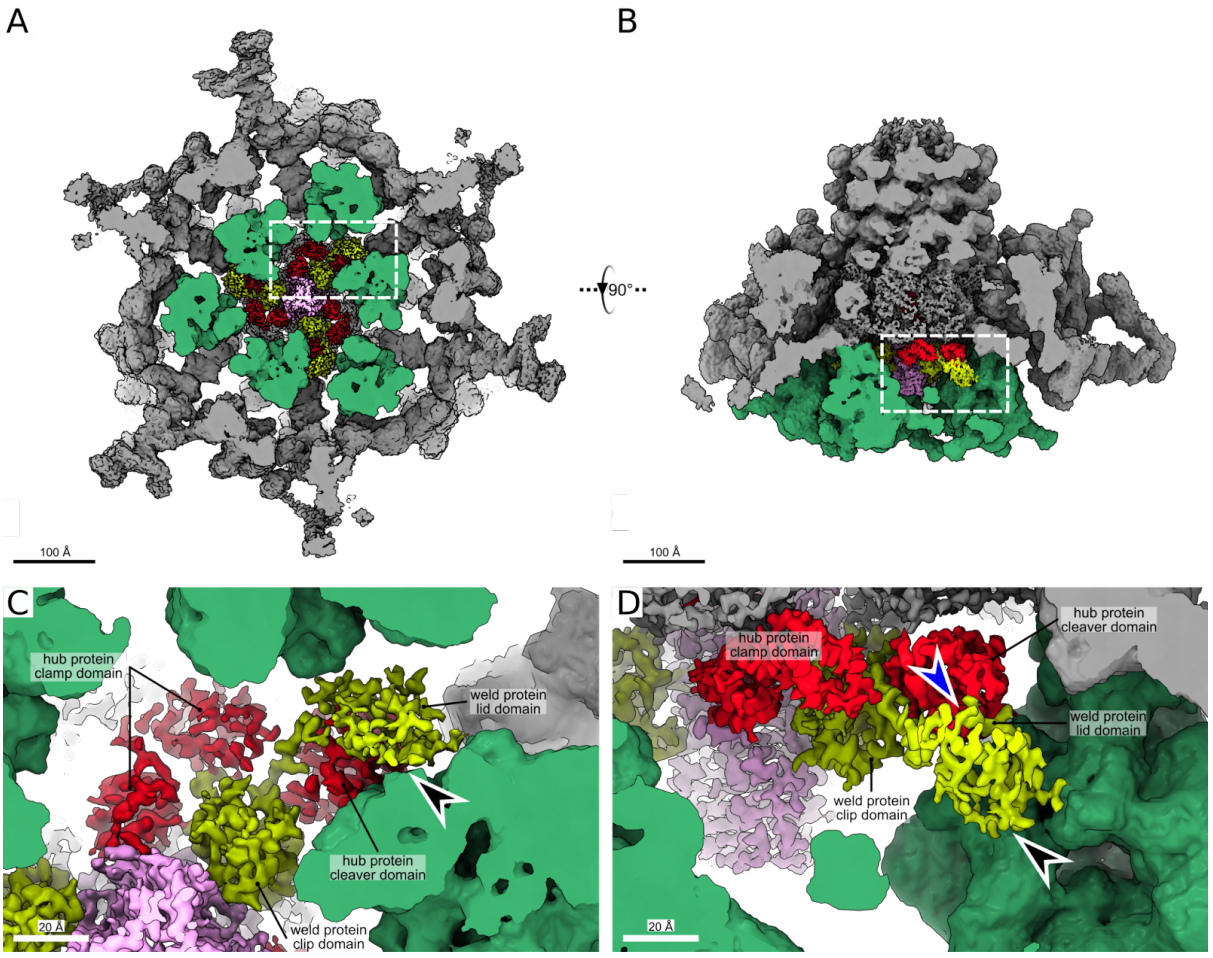

SFig. 9. Interactions of weld proteins with baseplate. The surface representation of the composite cryo-EM map of the phi812 baseplate is viewed along the tail axis towards the phage head **(A, C)**, and perpendicular to the tail axis **(B, D)**. Baseplate proteins are shown in gray except for the hub protein in red, the weld protein in light green, the central spike protein in pink, and the inner tripod proteins in dark green. The front density in panels A and B has been clipped away to show the interactions of the weld protein with the rest of the baseplate. Rectangles in A and B indicate close views, as shown in (C) and (D). Black arrowheads in C and D point to the interaction between the lid domain of the weld protein and the inner tripod protein. The blue arrowhead in D points to the site where the lid domain of the weld protein covers the active site of the cleaver domain of the hub protein. The names of domains of hub and weld proteins are indicated.

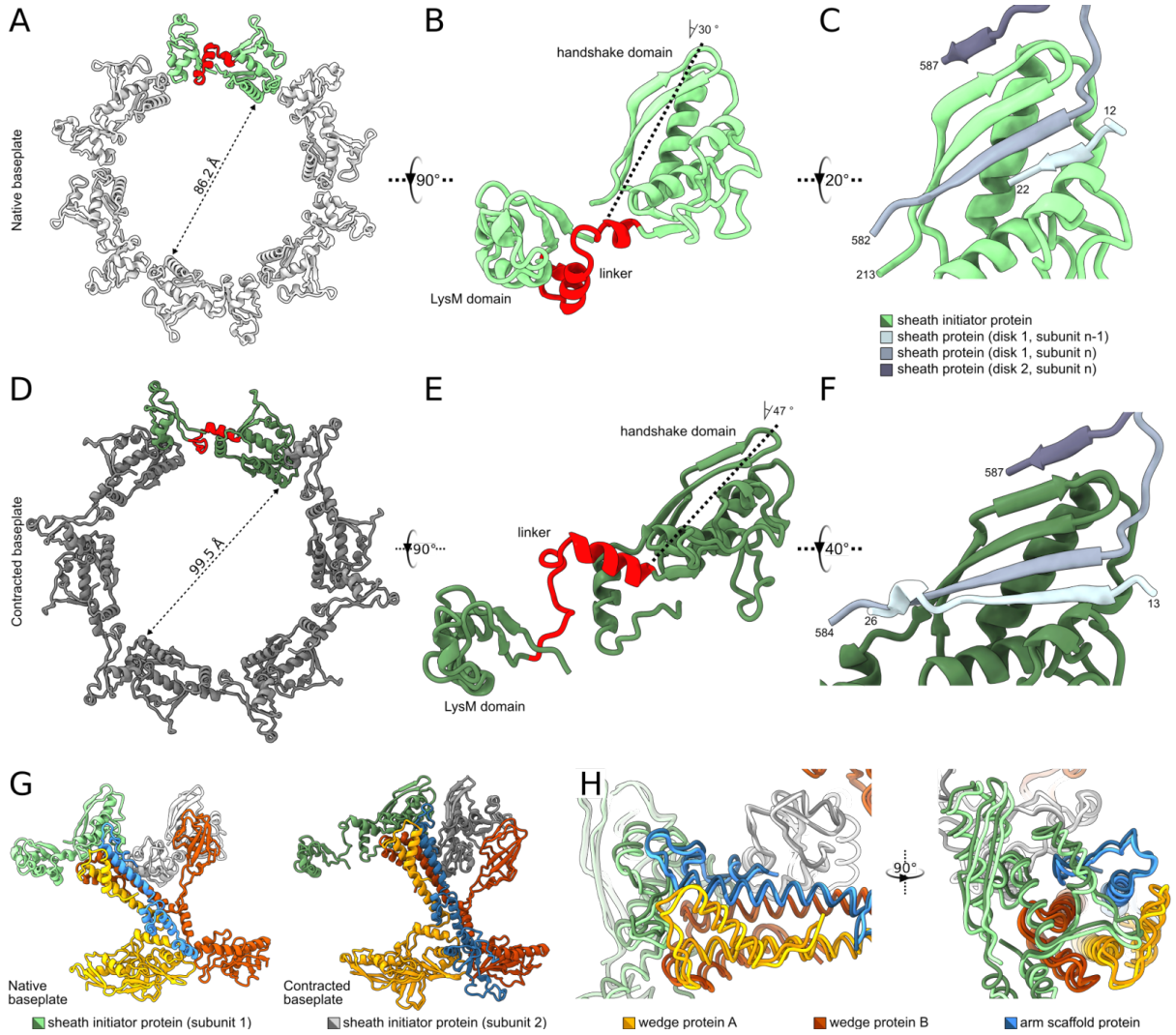

SFig. 10. Conformational changes and β-sheet augmentation of handshake domain of tail sheath initiator protein. (A-C) Cartoon representation of the tail sheath initiator protein from the native phi812 baseplate. (A) Five subunits from the hexamer of the tail sheath initiator proteins are shown in light gray, and one subunit in light green, with the linker between the LysM and handshake domains in red. (B) The structure of the tail sheath initiator protein with the linker between the LysM and handshake domains is shown in red. The angle between the tail axis and the axis of the handshake domain is indicated. (C) Augmentation of the β-sheet of handshake domain of the tail sheath initiator protein in the native phi812 baseplate with β-strands formed by an N-terminus and C-termini from three tail sheath proteins colored in three shades of gray. **(D-F)** Structure of tail sheath initiator proteins from the baseplate of phi812 with a contracted tail. (D) The hexamer of the tail sheath initiator proteins with five subunits is shown in dark gray, and one subunit in dark green with the linker between the LysM and handshake domains in red. (E) Structure of the tail sheath initiator protein. (F) Augmentation of the β-sheet of handshake domain of tail sheath initiator protein in phi812 with a contracted tail with β-strands formed by an N-terminus and C-termini from three tail sheath proteins colored in three shades of gray. **(G)** Interactions of tail sheath initiator proteins and a wedge module in native and contracted baseplates. **(H)** Differences between the interactions of tail sheath initiator proteins and wedge modules in native and contracted baseplates.

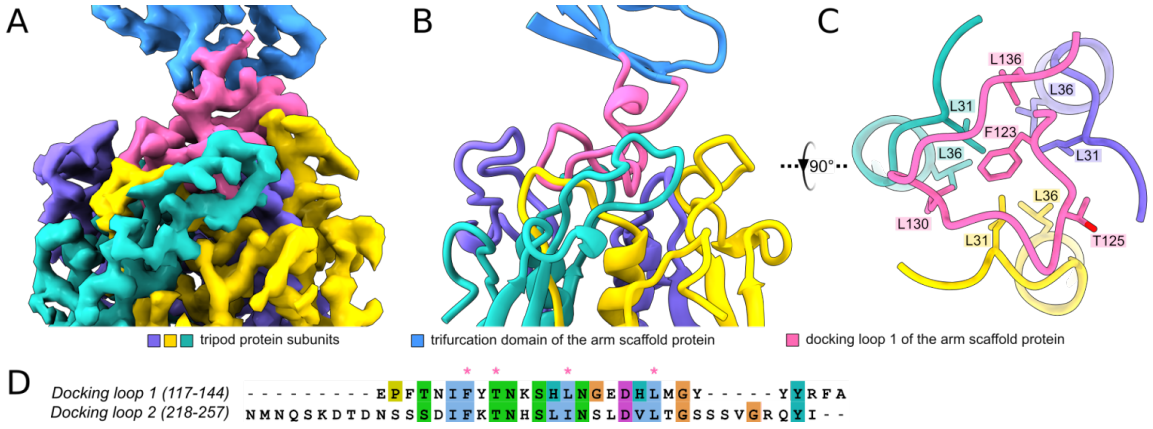

SFig. 11. Mechanism of binding of inner tripod trimer to arm scaffold protein. (A) Surface representation of cryo-EM map of the interface between the inner tripod complex and the arm scaffold protein from phi812 with a contracted tail. Tripod proteins and parts of the arm scaffold protein are colored according to the legend at the bottom. **(B)** The same as A, with the interaction partners shown in cartoon representation. **(C)** Top view of the interaction between the three tripod proteins and docking loop 1 of the arm scaffold protein. Side chains of the residues contributing to the hydrophobic interaction are shown as sticks. **(D)** Sequence alignment of docking loops 1 and 2 of the arm scaffold protein. Pink asterisks indicate residues of docking loop 1 participating in the interaction with the tripod proteins, as shown in panel C.

```
Tripod hook domain (613-670) ----TEQKTKKVTMKRFWRHNESYYGETEHYLYSNLQLDAG---QKWKGETYAYDR---EHGRTGTLLESG---------------
2mpw LTHNSYQNRLFYTLKT---------GETVADLSKSQDINL--------STIWSLNKHLYSSESEMMKAAPGQQIILPLKKL-----
2mtz -----GRKLLTYQVKQ---------GDTLNSIAADFRIST--------AALLQAN----PSLQAG--LTAGQSIVIPGLPD-PYTI
3zqd -----GRKLLTYQVKQ---------GDTLNSIAADFRIST--------AALLQAN----PSLQAG--LTAGQSIVIPGLPD-PYT-
4a1i -------GMLTYQVKQ---------GDTLNSIAADFRIST--------AALLQAN----PSLQAG--LTAGQSIVIPGLPD-PYTI
4b8v C---GSTSNIKYTVVK---------GDTLTSIAKKFKSGI--------CNIVSVN-----KLANPNLIELGATLIIPENCSNPDN-
7pvc -------ASQFYTVKS---------GDTLSAISKQVYGNAN-----LYNKIFEANK---PMLKSPDKIYPGQVLRIPEEL------
7vcm ------TASQFYTVKS---------GDTLSAISKQVYGNAN-----LYNKIFEANK---PMLKSPDKIYPGQVLRIP---------
7r1l ----------MYTVKP---------GDTMWKIAVKYQIGI--------SEIIAAN----PQIKNPNLIYPGQKINIP---------
4s3k -----PINGTYYTVKA---------GDTIWKVGRKLGVSY--------QAIANAN-----NVSVTAPLTPGRRILIPPSPN-----
4pxv -------CT-TYTIKS---------GDTCYAISQARGISL--------SDFESWN-----AGIDCNNLQIGQVVCV----------
5ylg -------CT-TYTIKS---------GDTCYAISQARGISL--------SDFESWN-----AGIDCNNLQIGQVVCVSK--------
5bum -------CTSYYTVKS---------GDICYNIAQTYGIDV--------ATLQSYN-----PGLQCDNLQIGQQLCVAD--------
4uz3 --------QATYTVAP---------GDTLYSIARRYGTTV--------EELMRLN------GLESFLLQPGQVLKLPS--------
5k2l -------MGCTYTIQP---------GDTFWAIAQRRGTTV--------DVIQSLN-----PGVNPARLQVGQVINVPC--------
5c8p -------STATVTVQQ---------GDTLRDIGRRFDCDF--------HEIARRN-----NIQNEDLIYPGQVLQVGG--------
5jcd ----QSDRLPIYVVQP---------QDGLDAIARNVFNAFV-----TYQEIAAAN-----NIPDPNKINVSQTLWIPL----P---
4eby ----CPLALASYYLEN---------GTTLSVINQNLNSSIAPYDQINFDPILRYN----SNIKDKDRIQMGSRVLVPF----PC--
7bax ----NSFSNISHMIKE---------GESYYYLSTTSYENLT-----NWETVQDSN-----PNYNPYLLPVGIKVVIPLFCK-----
```

SFig. 12. Hook domain of tripod protein shares conserved residues with proteins from LysM family. Primary sequence alignment of residues 613-670 forming the hook domain, with LysM protein family members (PDB codes are listed).

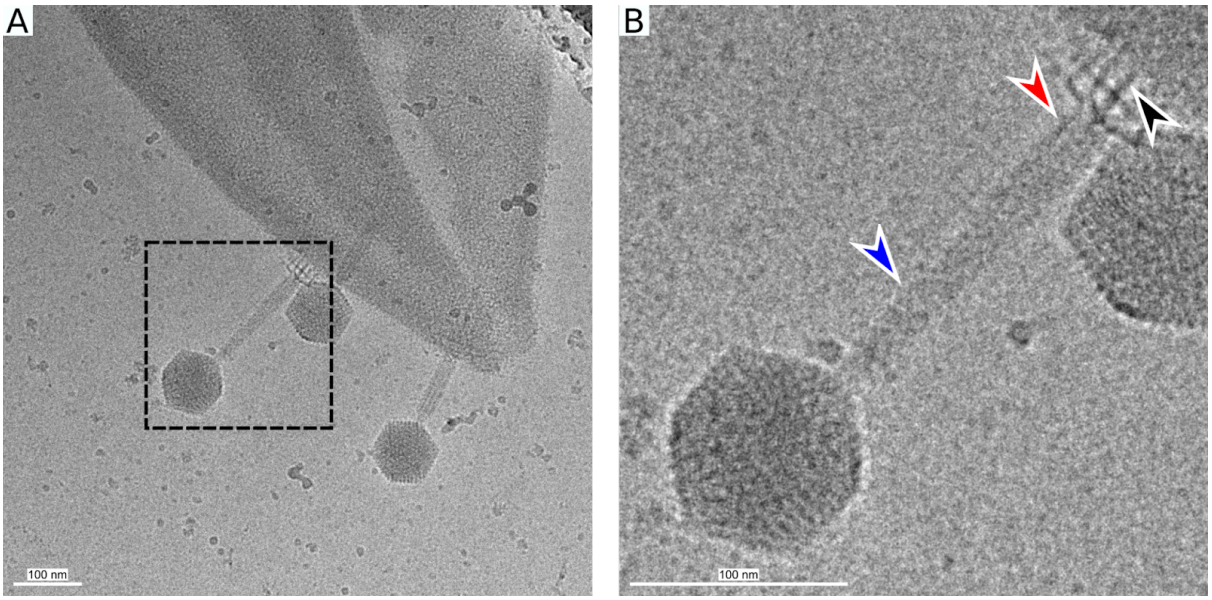

SFig. 13. Particle of phage phi812 captured in intermediate state of tail contraction. (A) Cryo-electron micrograph of phi812 attached to a cell wall of *S. aureus*. The black rectangle indicates the detail in B. **(B)** phi812 particle with a semi-contracted tail sheath. The blue arrowhead points to the sheath in the native conformation, whereas the red arrowhead points to the sheath in the contracted conformation. The black arrowhead points to the densities at the bottom of the contracted baseplate, presumably belonging to the anchor and hook domains of tripod proteins.

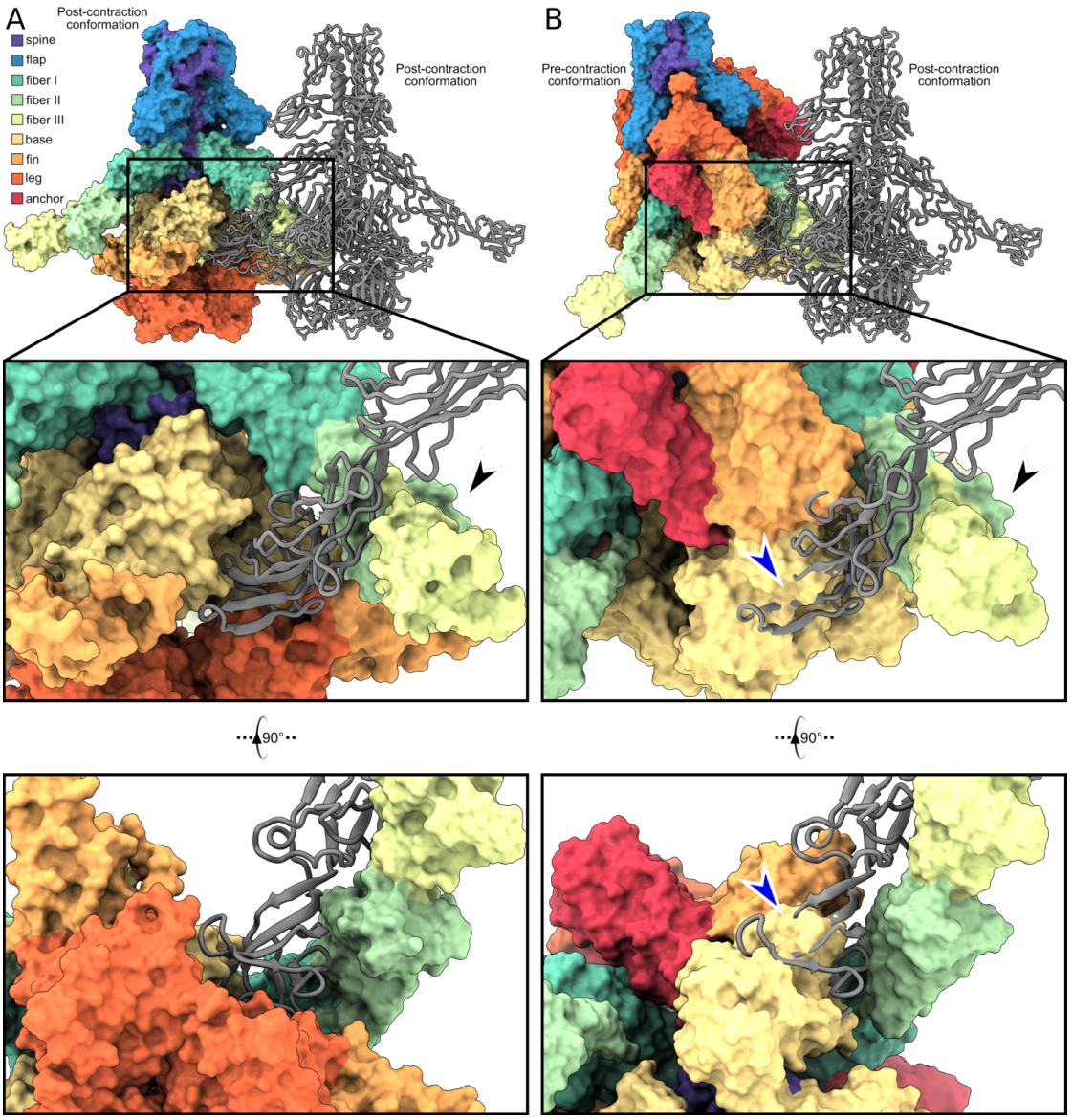

SFig. 14. Interactions between tripod complexes in baseplate of phi812 particle with contracted tail. (A) Interactions between two neighboring inner tripod complexes. One tripod complex is shown as a molecular surface colored according to domain, and the other is shown in cartoon representation in gray. The black rectangle indicates the magnified view shown in the insets below. The upper inset shows the interactions between fiber domains viewed perpendicular to the tail axis, and the lower inset shows the view along the tail axis toward the phage head. The black arrowhead points to the fiber domains of a tripod protein subunit used to superimpose the tripod complex in the pre-contraction state, as shown in B. **(B)** The inner tripod complex in the pre-contraction conformation is shown as a molecular surface colored according to domain, and the tripod complex in the post-contraction state is shown in gray cartoon representation. The pre-contraction tripod complex was superimposed onto the post-contraction tripod complex using the fiber domains indicated by the black arrowhead. The black rectangle indicates the close view shown in the insets below. The upper inset shows the view perpendicular to the tail axis, and the lower inset shows the view along the tail axis and towards the phage head. Blue arrowheads point to the site where the fiber III domains of the post-contraction tripod complex clash with the base domain of the pre-contraction tripod complex.

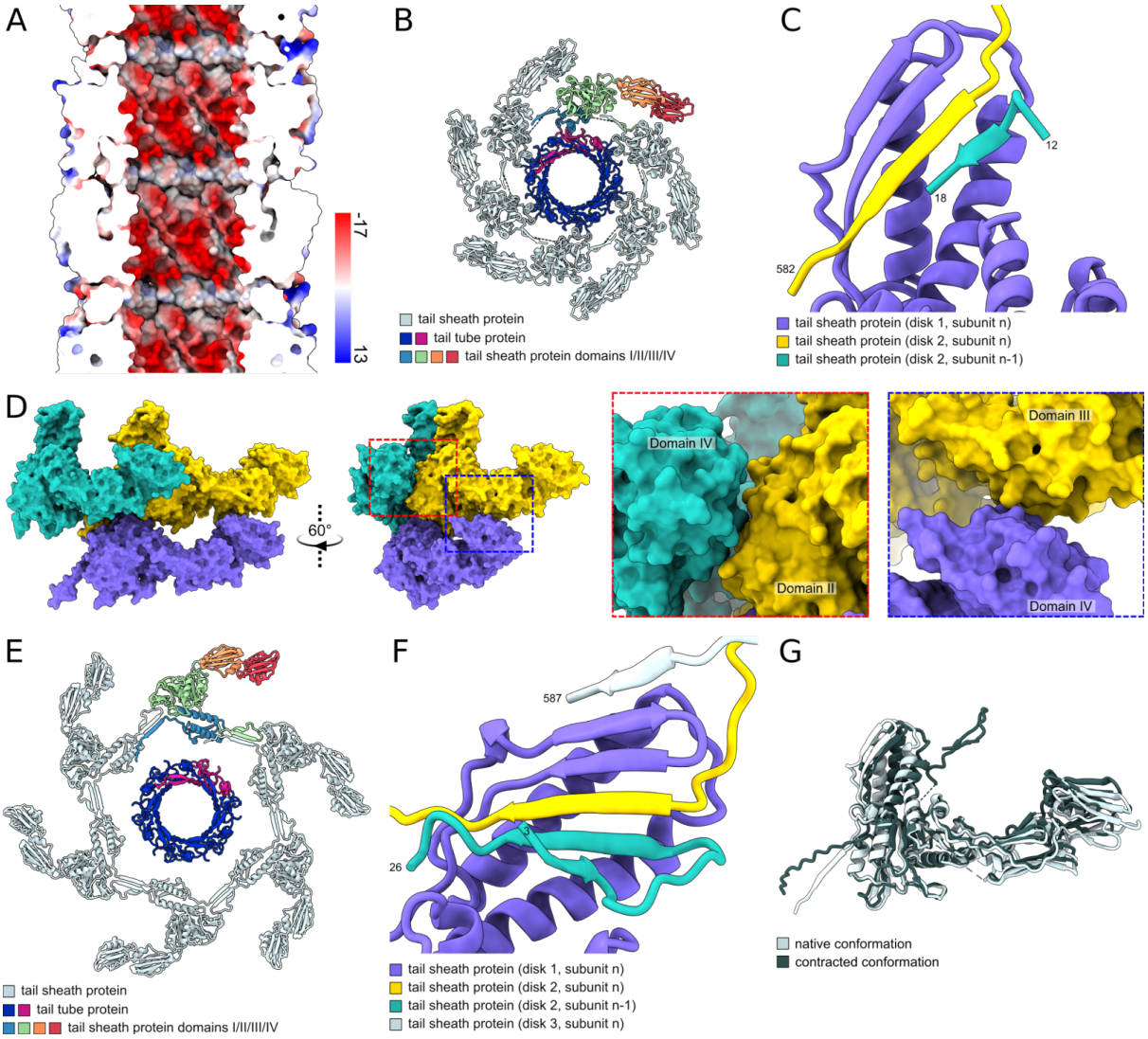

SFig. 15. Tail tube and tail sheath proteins. (A) Molecular surface representation of the phi812 tail tube with the front half removed and colored according to Coulombic electrostatic potential in the range from -17 to 13 kcal/(mol·*e*-) at 298 K. **(B)** Cartoon representation of a disc of tail tube and tail sheath proteins from the native phi812 tail viewed along the tail axis towards the phage head. Protein subunits are colored according to the legend. **(C)** β-sheet augmentation of the handshake domain of the tail sheath protein in native conformation with the N-terminus and two C-termini from other tail sheath proteins. The number of terminal residues of the displayed structures are indicated. **(D)** Molecular surface representations of three tail sheath proteins in their native conformation. Red and blue dashed rectangles indicate views of interactions among the subunits shown on the right at higher magnification. **(E)** Cartoon representation of a disc of the tail tube and tail sheath proteins from the contracted tail viewed along the tail axis towards the phage head. The relative rotation of the tail tube disc against the sheath disc is arbitrary. The proteins are colored according to the legend. **(F)** β-sheet augmentation of the handshake domain of the tail sheath protein from the contracted tail. Terminal residues are indicated. **(G)** Comparison of the tail sheath proteins from native (light gray) and contracted (black) tails. The subunits were superimposed by aligning their domains II.

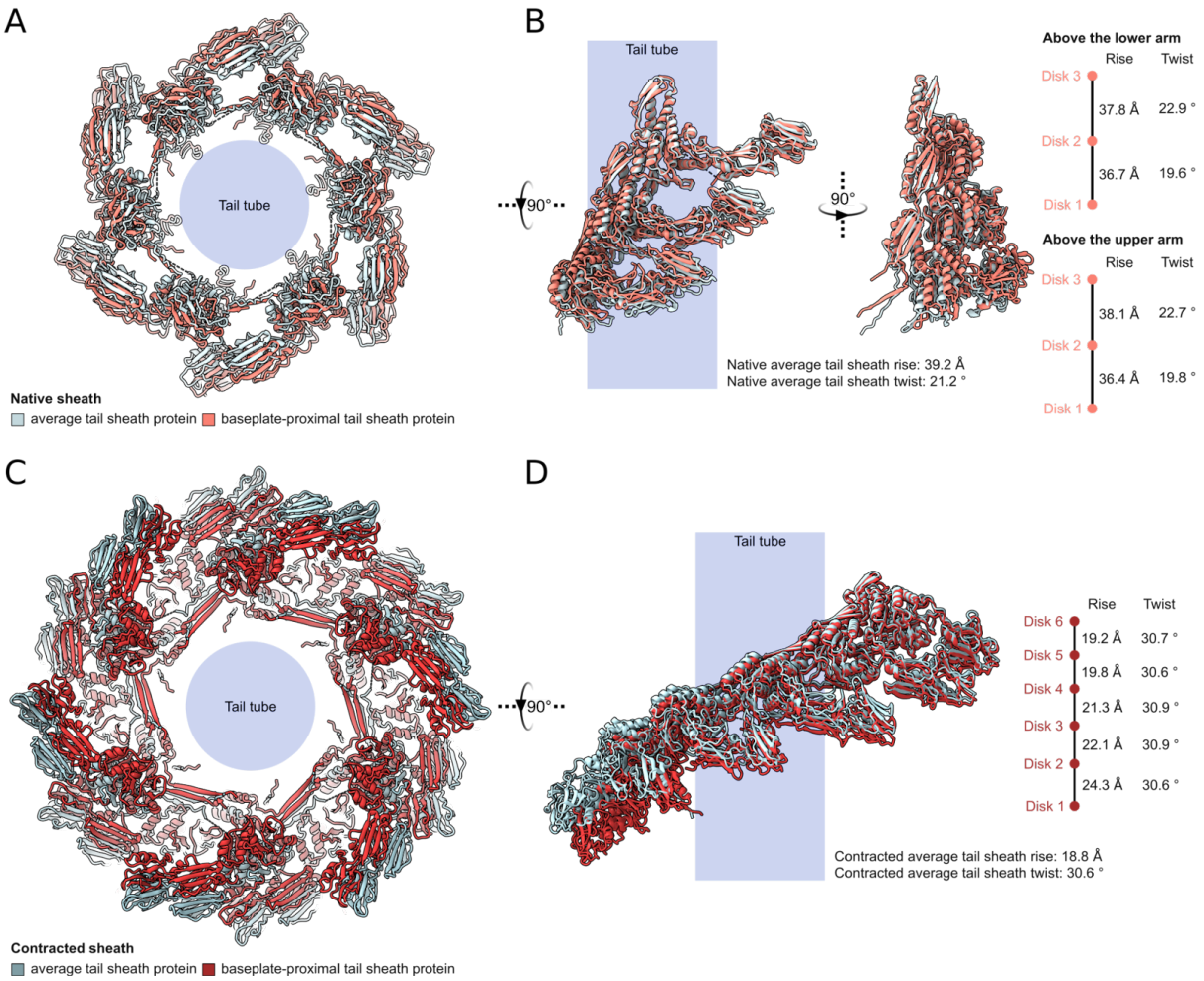

SFig. 16. Baseplate-proximal discs of tail sheath proteins of phi812 in native and contracted states deviate from respective tail sheath structures at the center of the tail. (A) Comparison of the cartoon representations of three baseplate-proximal tail sheath discs to three tail sheath discs from the central part of the tail. The structures are viewed along the tail axis towards the phage head. The position of the tail tube is indicated. Rise and twist differences were determined by superimposing domains I of tail sheath proteins from the uppermost discs (see Materials and Methods section for details). **(B)** Comparison of distances between tail sheath proteins from three baseplate-proximal tail sheath discs to three tail sheath discs from the central part of the tail. The twist and pitch parameters are indicated. **(C)** Comparison of the cartoon representations of six baseplate-proximal contracted tail sheath discs to six tail sheath discs from the central part of the tail. The structures are viewed along the tail axis towards the phage head. The position of the tail tube is indicated. **(D)** The scene from panel C viewed perpendicularly to the tail axis. Only six tail sheath proteins from each average and baseplate-proximal tail sheath protein discs are shown. The rise and twist difference between tail sheath subunits from successive discs is indicated on the right.

Supplementary movies

SMovie 1. Core proteins and wedge modules of the baseplate of phi812 in native conformation. The baseplate core and wedge module proteins are shown in cartoon representation and colored according to Fig. 1E. The wedge module in the native conformation 1 is shown in lighter colors to emphasize two distinct conformations of the wedge modules in the native phi812 baseplate. The superposition of two neighboring wedge modules in native conformation 1 and native conformation 2 is shown. Protein names are indicated.

SMovie 2. Baseplate and baseplate-proximal tail of phi812 in native conformation. The baseplate and baseplate-proximal part of the tail of phi812 in native conformation are shown in cartoon representation and colored according to Fig. 1E.

SMovie 3. Conformational changes of the baseplate arm of phi812. The baseplate and baseplate-proximal part of the tail of phi812 in native and contracted conformations are shown in cartoon representation. Conformational changes to a single baseplate arm are shown.

SMovie 4. Conformational changes of the tripod complexes. The tripod protein complexes of phi812 in native and contracted conformations are shown in cartoon representations colored by subunits and by domain.

SMovie 5. Conformational changes of the wedge modules, tail sheath initiator, and baseplate-proximal tail sheath proteins of phi812. The baseplate and baseplate-proximal tail of phi812 in native and contracted conformations are shown in cartoon representation. Conformational changes of the wedge module, tail sheath initiator, and baseplate-proximal tail sheath proteins are shown.

Supplementary Tables

Table S1. Cryo-EM data and structure quality indicators.

	Native tail	**Native baseplate (core, wedge modules, arms, proximal tail)**	**Native baseplate (core, wedge modules, proximal tail)**	**Native baseplate (core, wedge modules)**	**Contracted baseplate (core, wedge modules, arms, proximal tail)**	**Contracted baseplate (core, wedge modules, arm segment, inner tripods, proximal tail)**	**Contracted baseplate (core, wedge modules, inner tripods)**	**Contracted tail tube**	**Contracted tail sheath**	**Central spike protein (knob and petal domains)**
Sample	Native particles	Native particles	Native particles	Native particles	Contracted particles	Contracted particles	Contracted particles	Contracted particles	Contracted particles	Recombinant central spike protein
Data collection and processing										
Detector	Falcon 2	Falcon 2	Falcon 2	Falcon 2	K2 Summit	K2 Summit	K2 Summit	K2 Summit	Falcon 2	K2 Summit
Magnification	75,000	75,000	75,000	75,000	130,000	130,000	130,000	130,000	75,000	130,000
Voltage [kV]	300	300	300	300	300	300	300	300	300	300
Exposure [$e^-/Å^2$]	48	48	48	48	42	42	42	42	48	42
Pixel size [Å]	1.061	1.061	1.061	1.061	1.057	1.057	1.057	1.057	1.061	1.04
Symmetry	C6	C3	C3	C3	C6	C6	C6	C6	C6	C3
Initial number of particles	43,718	23,421	23,421	23,421	54,841	54,841	54,841	25,203	106,091	226,791
Final number	18,188	9,709	9,709	9,709	25,203	25,203	25,203	12,906	69,969	135,736

of particles										
Initial model	EMD-4051	EMD-8210	EMD-8210	EMD-8210	EMD-8212	EMD-8212	EMD-8212	Reconstructed particles with subtracted signal	EMD-4052	De novo
Map resolution [Å]	4.2	7.3	4.6	4.4	4.4	4.0	3.1	3.7	3.2	3.2
FSC threshold	0.143	0.143	0.143	0.143	0.143	0.143	0.143	0.143	0.143	0.143
Accession codes										
EMDB	EMD-50093	EMD-19968	EMD-19969	EMD-19970	EMD-19971	EMD-19972	EMD-19973	EMD-50094	EMD-50095	EMD-19974
PDB	9F04	9EUF	9EUG	9EUH	9EUI	9EUJ	9EUK	9F05	9F06	9EUL
Model composition										
Atoms (except hydrogens)	20,968	160,501	62,532	30,906	92,222	56,898	29,740	3,330	34,568	9,132
Residues	2,680	30,231	7,900	3,856	12,485	7,232	3,756	423	4,424	1,146
B-factors	89.62	48.40	69.46	49.03	64.71	71.54	49.55	54.95	98.49	69.58
FSC model 0.5 (masked)	4.19	10.38	4.60	6.21	6.65	4.14	3.25	3.86	3.30	3.27
RMSD										
Bond length [Å]	0.005	0.012	0.007	0.003	0.008	0.006	0.005	0.001	0.002	0.002
Bond angles [°]	0.726	1.998	1.027	0.471	1.400	0.881	0.781	0.404	0.437	0.438

Validation										
MolProbity score [percentile]	0.94	1.51	1.44	1.18	1.04	1.16	0.94	0.96	0.99	1.08
ClashScore [percentile]	0.96	0.99	1.72	2.67	1.05	1.23	0.90	1.96	2.19	2.71
Poor rotamers [%]	0.18	1.45	1.41	0.32	0.44	0.43	0.12	0	0	0
C-β outliers [%]	0	0.15	na	na	0.04	na	na	na	na	na
Ramachandran plot										
Outliers [%]	0	1.98	0.15	0.03	0.05	0.07	0	0	0	0
Favored [%]	97.13	88.30	94.06	97.35	96.42	95.40	97.07	99.04	98.35	97.89

824 na = not applicable

825 **Table S2. List of structural proteins from phi812 tail and baseplate.**

ORF	protein	residues	domains (residue range)	representative homologs
101	Tail sheath	587	I (491-587)	Phage T4, gp18[3]; phage E217, gp31[4]; *V. cholerae* Type VI Secretion System, VipA/B[67]
			II (34-96,313-490)	
			III (97-151,251-312)	Prophage *L. innocua*, Lin1278, PDB: 3LML
			IV (152-250)	
102	Tail tube	142	β-barrel (1-34,59-142)	Phage T4, gp19[3]; *P. aeruginosa* R2 pyocin, PA0626[22], *C. difficile* diffocine, CD1364[27]
			stacking loop (35-58)	
110	Hub	810	tube-forming I (1-125)	Phage T4, gp27[36]; *E. coli* Type VI Secretion System, VgrG[40]; *P. aeruginosa* R2 pyocin, PA0628[22]; phage 80alpha, ORF59[38]
			tube-forming II (126-266)	
			tube-forming III (267-285,546-641)	
			tube-forming IV (286-334,527-545)	
			clamp (358-511)	*V. vulnificus*, PAS factor[46]
			cleaver (642-808)	Phage K, ORF56 (tail-associated lysin)[44]; phage K, LysK (endolysin)[43]
111	Weld	295	clip (1-128)	*R. typhi* Type IV Secretion System, VirB8[79]; *H. pylori* Type IV Secretion System, CagV[80]
			linker (129-142)	
			lid (143-295)	*B. cereus*, YkfC[81]; *M. tuberculosis*, RipD[47]
112	Central spike	848	oligosaccharide-binding (OB) (1-110)	Phage T4, gp5[36]; phage phi92, gp138 (spike)[35]
			β-prism (111-310)	
			coiled-coil (311-466)	Phage P22, gp26 (tail needle)[82]
			knob (467-610)	Phage Sf6, tail needle[83]; phage 1358, receptor-binding protein[30]; *B. cenocepacia,* BC2L-C (lectin)[32]
			petal (611-848)	*B. subtilis*, GlpQ (phosphodiesterase)[34]
113	Tail tube initiator	263	tube-like (1-156)	Phage T4, gp54/gp48[3]; *P. aeruginosa* R2 pyocin, PA0626 (ripcord)[22]; *C. difficile* diffocine, CD1367[27]

			handle (157-263)	*P. aeruginosa* R2 pyocin, PA0626 (ripcord)[22]; phage E217, gp37/gp38[4]; phage Pam3, gp17[6]
114	Assembly	173	-	*P. aeruginosa* R2 pyocin, PA0626 (ripcord)[22]; phage Milano, BCP (gp25)[9]
115	Tail sheath initiator	234	LysM (1-66)	Phage T4, gp53[3]; *P. aeruginosa* R2 pyocin, PA0627 (glue)[22]; phage Milano, BCP (gp25)[9]
			linker (67-92)	-
			handshake (93-234)	Phage T4, gp25[3]; *P. aeruginosa* R2 pyocin, PA0617 (sheath initiator)[22]; phage E217, gp34[4]; phage Pam3, gp17[6]
116	Wedge A, B	348	helices (1-67)	Phage T4, gp6[3]; *E. coli* Type VI Secretion System, TssFa/b[21]; *C. difficile* diffocine, CD1364[27]
			wing (68-192)	*C. difficile* diffocine, CD1364[27]; phage E217, gp44[4]; phage Milano, BCP (gp25)[9] ; phage A1(L), gp31[8]
			trifurcation unit (193-256)	Phage T4, gp6[3]; *E. coli* Type VI Secretion System, TssFa/b[21]; *C. difficile* diffocine, CD1364[27]
			dimerization (257-348)	
117	Arm scaffold	1019	helices (1-94)	Phage T4, gp7[3]; *E. coli* Type VI Secretion System, TssG[21]; *P. aeruginosa* R2 pyocin, PA0619 (Tri2)[22]; phage E217, gp45[4]; phage Pam3, gp23[6]
			trifurcation (95-116,145-176)	
			docking loop 1 (117-144)	
			linker AB (177-212)	-
			bulge (213-219,259-443)	*A. thermocellus*, Xyn10B (carbohydrate-binding module 22)[84]; *P. barcinonensis*, Xyn10C (carbohydrate-binding module 22)[85]
			docking loop 2 (220-258)	
			linker BC (444-489)	-
			elbow (490-776)	Phage Tuc2009, BppA (putative receptor-binding protein)[29]; *P. barcinonensis*, Xyn10C (family 22 carbohydrate-binding module)[85]
			linker Z (777-907)	-
			connector (908-1019)	*B. ovatus*, putative alpha-L-fucosidase, (4ZRX); *C. polysaccharolyticus*, family 16 carbohydrate-binding module[60]
118	Arm segment	173	-	Phage T4, gp8[3]; A511, gp105[18]
119	Tripod	1152	spine helices (1-54,172-189,468-495)	-
			flap (55-115,139-171)	Phage 1358, receptor-binding protein (shoulder)[30]; *E. coli* Type VI Secretion System, TssK[21]

			flap insertion loop (116-138)	
			fiber I (190-242,404-467)	
			fiber II (243-276,359-403)	*R. capsulatus* Gene Transfer Agent, adaptor[86]; phage YSD1, major tail protein (domain 2)[87]; phage CBA120, central spike (domain XD2/XD3)[88]
			fiber III (277-358)	
			base (496-538,1045-1152)	*C. polysaccharolyticus*, family 16 carbohydrate-binding module[60]; *T. maritima*, family 61 carbohydrate-binding module[59]
			fin (539-565,944-1044)	
			leg (566-590,793-943)	*C. difficile*, Cwp84 (lectin-like)[61]
			anchor (591-612,674-792)	SSV19, B120 (adaptor)[89]; *B. ovatus*, $BoSGBP_{MLG}$-B (Surface glycan-binding protein)[90]
			hook (613-673)	-
121	Receptor-binding protein 1	640	antenna (1-37)	-
			tower I (38-121)	Phage T4, gp34 (long tail fiber)[91]; *P. aeruginosa* R1 pyocin, PA0620 (fiber)[92]
			tower II (122-184,397-410)	
			wing (185-396)	Phage CBA120, tail spike protein 4[93]; *T. polysaccharolyticum*, Family 16 Carbohydrate-binding Module[60]
			tower III (411-514)	Phage T4, gp34 (long tail fiber)[91]; *P. aeruginosa* R1 pyocin, PA0620 (fiber)[92]
			tip (515-640)	Phage T7, gp17 (fiber)[94]
123	Receptor-binding protein 2	458	antenna (1-60)	-
			tower I (61-149)	Phage T4, gp34 (long tail fiber)[91]; *P. aeruginosa* R1 pyocin, PA0620 (fiber)[92]
			tower II (150-228)	
			tower III (229-327)	
			tip (328-458)	T7, gp17 (fiber)[94]

826

827 **Table S3. NMR data and structure quality indicators for cleaver domain of hub protein.**

Table Structural statistics of 20 models	**CHAP**
NMR distance and dihedral restraints	
Distance restraints	
Total NOE	1632
Intra-residue (*i*=*j*)	460
Sequential (|*i* – *j*| = 1)	439
Medium-range (1 < |*i* – *j*| < 5)	223
Long-range (|*i* – *j*| > = 5)	510
Total dihedral angle restraints	195
φ	95
ψ	100
Violations (mean ± s.d.)	
Distance restraints (Å)	0.020 ± 0.002
Dihedral angle restraints (º)	0.808 ± 0.085
Max. dihedral angle violation (º)	5.72
Max. distance constraint violation (Å)	0.946
Deviations from idealized geometry	
Bond lengths (Å)	0.011± 0.000
Bond angles (º)	1.12± 0.032
Impropers (º)	1.88 ± 0.071
Average pairwise r.m.s. deviation* (Å)	
Backbone	0.99 ± 0.26
Heavy	1.36 ± 0.23
Ramachandran plot statistics* (%)	
Residues in most favoured regions	96.9
Residues in additionally allowed regions	2.7
Residues in generously allowed regions	0.1
Residues in disallowed regions	0.3

828 * Ordered residues: 25-42, 51-100, 103-129, 135-159

Table S4. X-ray data and structure quality indicators.

Data collection	Arm segment protein
Space group	P2(1)
Cell axes a, b, c [Å]	92.93, 75.14, 94.45
Cell angles α, β, γ [°]	90.00, 109.87, 90.00
Beamline	Soleil, Proxima 2A
Resolution range [Å]	46.49-1.80
Reflections	109 411
Completeness [%]	96.07
Mean <I/s(I)>	1.13
R_{merge} [%]	0.146
Wilson B [$Å^2$]	38.12
Refinement	
Reflections R_{free}	5471
R-factor	0.245
R-free	0.275
Overall B-factor [$Å^2$]	43.51
Ramachandran stats [%]	98.16
rmsd bonds (Å)/angles [°]	0.011; 1.146
PDB code	9FKO

Materials and Methods

Bacteriophage propagation and purification

Phage phi812, strain K1/420 (GenBank Accession Number KJ206563.2), was propagated in *S. aureus* SA 812 planktonic culture and purified on a CsCl gradient as described before[17], then dialyzed against phage buffer (50 mM Tris pH 8, 10 mM NaCl, 10 mM $CaCl_2$).

Induction of phi812 tail contraction and genome release *in vitro*

To induce contraction of the phi812 tail, a previously reported protocol[95]o was modified. The purified phage sample (10^{12} PFU/ml) in phage buffer was supplemented with teichoic acid from *Staphylococcus aureus* (SIGMA) at a concentration of 100 µg/ml, then diluted 10x using a solution of 3M urea in the phage buffer and incubated at 42°C for 45 min. After incubation, the sample was diluted 3x in the phage buffer and treated with Turbonuclease (Abnova) at a final concentration of 3.5 U/ml for 15 min at room temperature. Phage particles were pelleted by centrifugation at 75,000 x *g* at 4°C for 1 h using a 50.2 Ti rotor (Beckman Coulter) and resuspended in the phage buffer.

Identification of structural proteins of phage baseplate

The purified phi812 phage was resuspended in Laemmli buffer and boiled for 3 min. Subsequently, the sample was treated with Turbonuclease (Abnova) at a final concentration of 2 U/µl for 15 min at room temperature. Proteins from the phage particles were separated using tricine gradient gel electrophoresis. Major protein bands were cut from the gel and used for mass spectrometry analysis. Mass spectrometry data processing and analyses were performed using FlexAnalysis 3.4 and MS BioTools (Bruker Daltonics). Mascot software (Matrix Science, London, UK) was used for sequence searches in exported MS/MS spectra against the National Center for Biotechnology Information database and a local database supplied with the expected protein sequences. The mass tolerance of peptides and MS/MS fragments for MS/MS ion searches were 50 parts per million and 0.5 Da, respectively. The oxidation of methionine and propionyl-amidation of cysteine as optional modifications and one enzyme mis-cleavage were set for all searches. Peptides with a statistically significant peptide score ($P < 0.05$) were considered.

Cryo-electron microscopy sample preparation, data collection, motion correction, and CTF estimation

Purified phi812 (10^{11} PFU/ml) in phage buffer (4 µl), either in the native or contracted state, was pipetted onto a holey carbon-coated copper grid (R2/1, mesh 200; Quantifoil), blotted and vitrified by plunging into liquid ethane using a Vitrobot Mark IV (FEI). The vitrified sample was transferred to a Titan Krios electron microscope (Thermo Fisher) operated under cryogenic conditions and at an acceleration voltage of 300 kV. The beam was aligned for parallel illumination in NanoProbe mode, and coma-free alignments were performed to remove the residual beam tilt.

Micrographs of phi812 virions were collected at a magnification of 75,000 x using a Falcon 2 direct electron detector (FEI) operating in linear mode, resulting in a calibrated pixel size of 1.061 Å/pix. Imaging was done under low-dose conditions (total dose 48 e-/Å2) and with defocus values ranging from −0.8 to −3.0 µm. A one-second exposure was fractionated into 18 frames and saved as a movie.

Micrographs of phi812 in a contracted state were collected at a magnification of 130,000 x using a K2 Summit direct electron detector (Gatan) operating in counting mode, resulting in a calibrated pixel size of 1.057 Å/pix. Imaging was done under low-dose conditions (total dose 42 e-/Å2) and with defocus values ranging from −1.0 to −2.4 µm. A seven-second exposure was fractionated into 40 frames and saved as a movie.

Automated data acquisitions were performed using the software EPU (Falcon 2) or Serial EM (K2 Summit). The movies were corrected for global and local motion during acquisition using MotionCor2[96], and saved as dose-weighted micrographs. Defocus values were estimated from aligned non-dose-weighted micrographs using the program Gctf[97].

Reconstruction of native baseplate of bacteriophage phi812

A total of 7,187 micrographs of phi812 virions were used to pick 23,421 particles using the e2boxer program from the EMAN2 suite[98]. Particles were then extracted and binned 4x to a 210 px box size (4.244 Å/px) using Relion[99]. The particles were subjected to several rounds of 2D and 3D classification with three-fold symmetry imposed, using the previously reconstructed native baseplate (EMD-8210) as an initial model lowpass-filtered to 60 Å.

The resulting 9,705 particles were re-extracted using an 840px box (1.061 Å/px) and auto-refined with C3 symmetry imposed and masking using Relion[100]. Next, several rounds of CTF refinements were performed, including an anisotropic magnification estimation and fitting of the defocus and astigmatism parameters per particle and micrograph, respectively. The resulting map of the baseplate reached a resolution of 7.3 Å after the post-processing, with a calibrated pixel size of 1.075 Å/px applied. Then, alternating rounds of 3D auto-refinement and CTF refinement were performed using a mask including the first three tail sheath rings, core, and wedge proteins, yielding a map with a resolution of 4.5 Å and a calibrated pixel size of 1.075 Å/px.

To improve the reconstruction of the core and wedge proteins, particles were re-extracted into a 300 px box (1.061 Å/px), and the reconstructed map was segmented to retain only the density corresponding to the core and wedge proteins. The sub-particles were then re-extracted into the same box with the offsets centered to x, y, and z coordinates equal to 0,0,-37 to account for the shift of the calculated center of mass along the Z axis. Re-centered particles were reconstructed, and an inverted mask was used to subtract the signal around the reconstructed map. After a 3D auto-refinement, additional 3D classification or CTF refinement did not improve the resolution. The final map was post-processed with a calibrated pixel size of 1.075 Å/px applied, reaching a resolution of 4.4 Å. In all the above cases, the resolution after post-processing was calculated according to the gold standard FSC = 0.143 criterion. The local resolution for each map was computed using Relion[101].

Reconstruction of phage phi812 with contracted tail

Out of 15,371 micrographs of phages in the post-contraction state, the first 1,000 micrographs were used to manually pick 7,539 particles using crYOLO[102]. Particles were then extracted and binned 4x to a 208 px box size (4.228 Å/px) using Relion[100]. After a single round of 2D classification, all aligned particles were re-extracted unbinned to a 832 px box size (1.057 Å/px) with re-centering of the offsets to x,y,z coordinates equal to 0,0,0. Then, particles were imported into Topaz[103] with a downsampling factor of 8. After training the neural network, the positions of particles were predicted using the radius r = 36 and picking threshold t = 0. The inspection of one hundred randomly selected micrographs with the respective particle coordinates in the crYOLO program revealed a negligible number of false negatives and false positives. After the picking coordinates were corrected for the sampling factor, 54,841 particles were extracted using a 960px box size and binned 4x (4.228 Å/px) using Relion[101]. After several rounds of 2D classification, 31,308 particles were subject to 3D reconstruction and classification with imposed C6 symmetry, using the previously reconstructed post-contraction baseplate (EMD-8212) lowpass-filtered to 60 Å as an initial model. The resulting 25,487 particles were re-extracted and binned 2x to obtain a 480 px box size (2.114 Å/px). After a 3D classification, one of the three classes exhibited the wrong handedness. Particles from this class were corrected using the xflip_particles_star.py script (github.com/fuzikt/starpy). After another round of 3D classification, 25,203 particles were used for the reconstruction, yielding a final map that reached the Nyquist resolution. Next, particles were re-extracted using a 960px box size (1.057 Å/px) and subjected to 3D auto-refinement using a whole-map mask. The final map reached a resolution of 4.4 Å after the post-processing. Next, 3D auto-refinement was performed using a focused mask that included the core and wedge proteins and an inner ring of tripod proteins. The resulting map reached a resolution of 4.11 Å after the post-processing. The particles were assigned to their respective optics groups, and several rounds of CTF refinements (anisotropic magnification estimation, beam tilt, trefoil, and tetrafoil aberrations estimation, and fitting of the defocus and astigmatism parameters per particle) improved the resolution of the map to 3.6 Å. Then, two rounds of Bayesian polishing and subsequent 3D auto-refinements and CTF refinements were performed. In the final post-processing step, a negative B-factor of -25 was applied to produce the final map with an average resolution of 3.1 Å. The final post-processing step was also performed using a mask encompassing the first six tail sheath discs, core and wedge proteins, inner ring of tripod proteins, and a subunit of the arm segment protein, resulting in a map with a resolution of 4 Å. The resolution was calculated according to the gold standard FSC = 0.143 criterion in all cases. The local resolution for each map was computed using Relion[101].

Reconstruction of native phi812 tail

The phi812 tails were manually boxed using the program e2helixboxer.py from the EMAN2 suite[98], and the helical segments were extracted in a 360 px box using Relion[100]. Tail edges and bent and damaged particles were removed from the dataset by multiple rounds of reference-free 2D classification. A map of the phi812 tail in its native conformation (EMD-4051) low-pass filtered to 50 Å was used as an initial model for the 3D auto-refinement of 18,188 particles using a helical refinement protocol with C6 symmetry imposed. The helical refinement and the per-particle CTF refinement were iterated until convergence. The final map reached a resolution of 4.2 Å. The

resolution after post-processing was calculated according to the gold standard FSC = 0.143 criterion. Local resolution maps were computed using Relion[101].

Reconstruction of contracted tail

A total of 106,091 particles were manually picked from 4,833 micrographs using the program e2helixboxer.py from the EMAN2 suite[98], and the helical segments were extracted using a 400 px box size (1.061 Å/px) in Relion[100]. Tail edges and bent and damaged particles were removed from the dataset by multiple rounds of reference-free 2D classification. Then, 85,549 particles were subjected to several rounds of 3D reconstruction and classification with C6 symmetry imposed. A map of the contracted tail determined previously (EMD-4052) filtered to 50 Å was used as an initial model for the 3D auto-refinement of 69,969 particles using a helical refinement protocol with C6 symmetry imposed. The final map reached an average resolution of 3.0 Å.

Localized reconstruction of tail tube from contracted baseplate

Information about particle positions and orientations from the final reconstruction of the baseplate of phages with contracted tails was used to extract sub-particle images of the tail tube with a modified localized reconstruction protocol[104] (github.com/fuzikt/localrec)). The initial set of 25,203 sub-particles (box size 256 px, 1.057 Å/pixel) centered on the contact region between the tail tube and wedge A proteins was subjected to several rounds of 2D classifications in Relion[101]. After the initial 3D auto-refinement with imposed C6 symmetry, a single 3D classification was performed. The selected 12,906 particles belonging to the best class were further auto-refined with imposed C6 symmetry and maximum allowed deviations from previous orientations of 10°. The final map reached an average resolution of 3.6 Å.

Production of recombinant cleaver domain of hub protein

The DNA segment encoding the cleaver domain of hub protein (residues 650-808) was amplified from the genomic DNA of phage phi812 by PCR using forward and reverse primers (5'GTAGCCATGGAACAAAGTAGTGGA3' and 5'TAGGATCCTTTATTTCTTATCGTAAA3'). Using restriction cloning, the amplicon was cloned into the vector pET28a(+) (Novagen/Merck), providing a T7 tag and a His6 tag at the C-terminus of the protein. An *E. coli* expression strain BL21(DE3) was transformed with the construct using a standard heat shock procedure (45 s at 42 °C). An overnight culture was used to inoculate 1 l of 2% Luria-Bertani broth (Oxoid) supplemented with kanamycin (50 µg/mL) and cultivated at 37 °C until OD_{600}=0.5. The protein expression was induced with 0.4 mM IPTG, and was allowed to progress for 4-6 h at 30°C.
For nuclear magnetic resonance spectroscopy (NMR), the cleaver domain was produced in M9 minimal medium supplemented with traces of metals, vitamins, and 2 g/L [^{13}C]glucose or 0.5 g/L $^{15}NH_4Cl$ (Cambridge Isotope Laboratories). *E. coli* BL21 (DE3) was grown to OD_{600} = 0.5, and the gene expression was induced with 0.4 mM IPTG and continued at 30 ºC for 12 h. The cultures were harvested, resuspended in the sonication buffer (100 mM Tris-Cl, pH 8, 500 mM NaCl, 4 mM DTT, 10 mM imidazole, 0.1 % TritonX-100), and subjected to sonication (Sartorius Labsonic® M), followed by centrifugation at 14,000 x *g* and 4 °C for 45 min. The supernatant was filtered (0.45 µm cut-off,

991 Corning Inc.) and loaded into a 5 ml Histrap column (GE Healthcare) pre-equilibrated with the loading
992 buffer and connected to an AKTA FPLC system (GE Healthcare). After the column was washed with 15
993 column volumes of the loading buffer (50 mM Tris-Cl, 300 mM NaCl, 20 mM imidazole), gradient
994 elution was performed using the elution buffer (50 mM Tris-Cl, 300 mM NaCl, 500 mM imidazole).
995 Fractions with protein were pooled, concentrated, and loaded onto a HiLoad 16/600 Superdex 75 pg
996 size-exclusion chromatography column (GE Healthcare Life Sciences), followed by an isocratic elution
997 with 100 mM Na-phosphate, pH 6.8, 150 mM NaCl. Purified protein was pooled, and the buffer was
998 exchanged by performing two washes with 20 mM Na-phosphate buffer, pH 6.8, using an Amicon
999 Ultra 15 filter (10 kDa cut-off, Millipore). While exchanging the buffer, the sample was concentrated
1000 to 20 mg/ml. For the NMR studies, the protein was concentrated at 35 mg/ml while
1001 buffer-exchanged to 25 mM Na-phosphate, pH 6.6, and 100 mM NaCl.
1002
1003 **Zymogram analysis**

1004 The cleaver domain of the hub protein after Histrap purification was separated on conventional
1005 12.5% polyacrylamide gel using SDS-PAGE. Polyacrylamide gels (12,5 %) for zymograms contained 0.5
1006 % bacterial cell walls, prepared from *S. aureus* CCM 885 cells, autoclaved at 121 ºC for 5 min.
1007 Samples of the cleaver domain were mixed with loading buffer (1% SDS, 6% sucrose, 100 mM
1008 dithiothreitol, 10 mM Tris, pH 6.8, 0.0625% bromophenol blue) and boiled for 5 min before loading
1009 onto SDS-PAGE gels and zymograms. The SDS-gel and zymogram were separated using gel
1010 electrophoresis. After the gel electrophoresis, the zymogram was washed for 30 min with distilled
1011 water to remove SDS. To renature the cleaver domain, the zymogram was soaked at room
1012 temperature in distilled water for 2-4 h, and then for 1 h in the buffer containing 150 mM
1013 Na-phosphate, pH 7.0, 0.1% Triton X-100 and 10 mM $MgCl_2$. The zymogram was stained for 3
1014 h with 0.1% methylene blue in 0.001% KOH and washed with water. The peptidoglycan-hydrolytic
1015 activity of the cleaver domain of the hub protein was detected as a clear zone on a dark blue
1016 background.
1017
1018 **NMR structure determination of cleaver domain of hub protein**

1019 NMR spectra were recorded at 298 K in an 850 MHz Bruker Avance III spectrometer equipped with a
1020 $^{1}H/^{13}C/^{15}N$ TCI cryogenic probe head with z-axis gradients. The composition of the NMR sample was
1021 1.8 mM uniformly ^{13}C-, ^{15}N-labeled cleaver domain in a buffer containing 25 mM sodium phosphate,
1022 pH 6.6, 100 mM NaCl, 1.5 mM DTT, and 10% D_2O for the lock. Three sparsely sampled 4D NMR
1023 experiments were acquired: 4D HC(CC-TOCSY(CO))NH, 4D $^{13}C,^{15}N$ edited HMQC-NOESY-HSQC (HCNH),
1024 and 4D $^{13}C,^{13}C$ edited HMQC-NOESY-HSQC (HCCH). Sequential and aliphatic side chain assignments
1025 were obtained automatically using the 4D-CHAINS algorithm[105] and checked manually. Backbone
1026 dihedral angle restraints were derived from TALOS[106] using a combination of five kinds (H^N, H^α, C^α, C^β,
1027 N) of chemical shift assignments for each residue in the sequence. NOE cross-peaks from the two 4D
1028 NOESY spectra (HCNH and HCCH) were assigned automatically by CYANA 3.0[107] in structure
1029 calculations with torsion angle dynamics. Unambiguous distance and torsion angle restraints (Table
1030 S3) were used in a water refinement calculation[108] applying the RECOORD protocol[109]. The quality of
1031 the NMR-derived structure ensembles was validated using PSVS[110].
1032

1033 **Production of recombinant central spike protein**

1034 The gene for central spike protein was amplified from the genomic DNA of phage phi812 using
1035 forward and reverse primers (5'AGATTGGTGGCTCGGATGATTTAAATGTAAAAGGATTAGTTTTA3' and
1036 5'GAGGAGAGTTAAGACTTATTAAATCTTTTTATATTCATCTAGGTAGTTTGTAAA3'). Compared to the
1037 full-length gene, the first 17 nucleotide triplets from the 5' end of the amplified gene were omitted,
1038 as they code for the first 17 residues of the central spike protein, which were predicted to be
1039 disordered by the secondary structure prediction using Phyre[111]. The truncated gene was cloned into
1040 a vector derived from pET22b, which was modified to provide a His6-SUMO-tag fusion followed by
1041 the Ulp1 cleavage site at the N-terminus of the protein. The *E. coli* expression strain BL21(DE3) was
1042 transformed with the construct using a standard heat shock procedure (45 s at 42°C). An overnight
1043 culture was used to inoculate 2% Luria-Bertani broth (Sigma) supplemented with ampicillin (50
1044 µg/ml). Cells were cultivated at 37°C and 250 rpm until OD_{600}=0.5, followed by cultivation at 16 °C
1045 and 250 rpm for 24 h without the induction of expression, as soluble central spike protein was only
1046 produced after non-induced leaky expression. Cells were harvested in a typical yield of 8 g per liter of
1047 cell culture, resuspended in 2.5 ml of the loading buffer (50 mM Na/K phosphate, pH 7, 200 mM
1048 NaCl) per g of cell pellet, and subjected to chemical disintegration (0.5 % octylthioglucoside, 1 mg/ml
1049 lysozyme, 2 U/ml Turbonuclease, 1 mM PMSF, 5 mM TCEP) at 6 °C overnight. The lysate was
1050 centrifuged at 20,000 x *g* and 8°C for 30 min. The resulting supernatant was filtered (0.45 µm cut-off,
1051 Corning Inc.) and loaded into a 5 ml Histrap column (GE Healthcare) pre-equilibrated with the loading
1052 buffer and connected to an AKTA FPLC system (GE Healthcare). After the column was washed with 15
1053 column volumes of the loading buffer, gradient elution was performed using the elution buffer (50
1054 mM Na/K phosphate, pH 7, 200 mM NaCl, 500 mM imidazole). Eluted fractions containing the central
1055 spike protein, as determined by SDS-PAGE analysis using 12.5 % polyacrylamide gels, were pooled
1056 and supplemented with 5 mM TCEP before the cleavage of the purification tag overnight at 6°C using
1057 the in-house prepared Ulp1 protease. The cleavage solution was desalted using a HiPrep™ 26/10
1058 Desalting column (Cytiva) before reverse affinity chromatography using the 5 ml Histrap column (GE
1059 Healthcare). Cleaved protein collected in the flow-through fraction was concentrated (30 kDa cut-off;
1060 Amicon ® Ultra; Merc Millipore) and loaded into a Superdex 16/600 200 pg column (GE Healthcare)
1061 pre-equilibrated with the loading buffer (50 mM Na/K phosphate, pH 7, 200 mM NaCl), followed by
1062 an isocratic elution. Monodisperse fractions were analyzed by SDS-PAGE and concentrated to a final
1063 concentration of 5 mg/ml.
1064

1065 **Cryo-EM reconstruction of recombinant central spike protein**

1066 The purified central spike protein sample was diluted in 50 mM Na/K phosphate, pH 7, 200 mM NaCl
1067 buffer to a concentration of 0.8 mg/ml, and then diluted 10x in water. Four µl of the central spike
1068 protein at a concentration of 0.08 mg/ml were applied onto a Quantifoil R1.2/1.3 200-mesh Cu grid
1069 glow-discharged for 60 s from both sides. The excess of the sample was blotted for 1 s with filter
1070 paper (Whatman No. 1) using blot force -2, and immediately plunge-frozen in liquid ethane using a
1071 Vitrobot Mark IV (FEI). The instrument chamber was kept equilibrated to 100 % humidity and at 4°C.
1072 Cryo-EM data were collected using a Titan Krios TEM (Thermo Fisher Scientific) operated at 300 keV
1073 and equipped with a K2 Summit direct electron detector (Gatan). The beam was aligned for parallel
1074 illumination in NanoProbe mode, and the residual beam tilt was removed by coma-free alignments.
1075 The software SerialEM was used to acquire the data in the electron counting mode at 130,000 x

1076 magnification, corresponding to a calibrated pixel size of 1.04 Å/px over a defocus range of -0.3 to
1077 -3.0 µm. The exposure of 8 s with a dose rate of 6.6 e^-/px/s was fractionated into 40 frames (total
1078 dose 57 $e^-/Å^2$, 1.425 $e^-/Å^2$ per frame). A total of 3120 micrographs were collected. For each movie,
1079 the drift and gain correction was performed with MotionCor2[96], while the contrast-transfer function
1080 was estimated using the program Gctf[97]. crYOLO[102] was used to pick particles from micrographs
1081 denoised using the program janni. Particles picked manually from 10 micrographs were used to train
1082 the neural network. The resulting 487,160 auto-picked particles were extracted and binned to a 128
1083 px box size using Relion[100]. Several rounds of 2D classification sorted out classes of the central spike
1084 protein's C-terminal domains containing 226,791 particles. These particles were re-extracted and
1085 binned to a 128 px box size (2.08 Å/px) using Relion 5.0 beta (github.com/3dem/relion/tree/ver5.0).
1086 Three more rounds of 2D classification resulted in 135,736 particles, which were used for 3D
1087 reconstruction using the initial model generated by the stochastic gradient descent algorithm within
1088 Relion. Subsequent 3D classifications did not improve the quality or resolution of the reconstruction.
1089 Therefore, all 135,736 particles were re-extracted using a 256 px box size (1.04 Å/px) and assigned to
1090 their respective optics groups. Several rounds of CTF refinements, including anisotropic magnification
1091 estimation, beam tilt and trefoil aberrations estimation, and fitting of the defocus and astigmatism
1092 parameters per micrograph, improved the resolution of the post-processed map to 3.65 Å. Then, two
1093 rounds of Bayesian polishing and subsequent 3D auto-refinements and CTF refinements were
1094 performed. The final map reached a resolution of 3.23 Å. The resolution after post-processing was
1095 calculated according to the gold standard FSC = 0.143 criterion. Local resolution maps were
1096 computed using Relion[101].
1097

1098 **Production of recombinant Arm segment protein**

1099 The gene encoding the arm segment protein was cloned into the pET-28b(+) vector
1100 (Novagen/Merck), providing a His6 tag at the C-terminus of the protein. An *E. coli* expression strain
1101 BL21(DE3) was transformed with the construct using a standard heat shock procedure (45 s at 42°C).
1102 An overnight culture was used to inoculate 2% Luria-Bertani broth (Sigma) supplemented with 1 mM
1103 MgCl2, 1 % glucose, and ampicillin (50 µg/ml), followed by cultivation at 37 °C and 250 rpm until
1104 OD_{600}=0.5. The expression was induced with 0.4 mM IPTG at 18°C, and was allowed to progress for
1105 17 h. Cells were harvested and lysed using the lysis buffer (0.5 % octyl-thioglucoside, 1 mg/ml
1106 lysozyme, 2 U/ml Turbonuclease, 1 mM PMSF, 5 mM TCEP) at room temperature for 30 minutes, and
1107 subsequently disintegrated with an Emulsiflex C3 (Avestin). After centrifugation at 20,000 x *g* and 8°C
1108 for 30 min, the supernatant was filtered (0.45 µm cut-off, Corning Inc.) and loaded into a 5 ml Histrap
1109 column (GE Healthcare) pre-equilibrated with the loading buffer (50 mM HEPES, pH 8, 200 mM NaCl,
1110 40 mM imidazole) connected to an AKTA Pure FPLC system (GE Healthcare). The protein was eluted
1111 in one step using the elution buffer (50 mM HEPES, pH 8, 200 mM NaCl, 500 mM imidazole). Eluted
1112 fractions containing the arm segment protein, detected by SDS-PAGE analysis on 12 %
1113 polyacrylamide gels, were loaded into a Superdex 16/600 75 pg column (GE Healthcare)
1114 pre-equilibrated with the loading buffer (50 mM HEPES, pH 8, 200 mM NaCl), followed by an isocratic
1115 elution. Monodisperse fractions were analyzed by SDS-PAGE and concentrated to a final
1116 concentration of 14 mg/ml.
1117

1118 **Crystallization and X-ray structure determination of recombinant arm segment protein**

1119 The arm segment protein was crystallized by vapor diffusion using the sitting-drop method at 21 °C.
1120 The protein sample at a concentration of 14 mg/ml was used to prepare drops with protein :
1121 precipitant ratios of 200 nl : 100 nl, 100 nl : 100 nl, and 100 nl : 200 nl in MRC 3-drop 96-well plates
1122 using a Dragonfly robot (SPT Labtech) with a range of commercially available screens (Molecular
1123 Dimensions, Hampton Research, Qiagen-Nextal). Thick needle-like crystals were observed in the
1124 drops containing the solution of 1.6 M LiCl, 0.1 M Tris, pH 7.5, 25 % w/v PEG 4,000. The same
1125 crystallization solution was used to prepare hanging drops for vapor diffusion. Crystals were
1126 harvested from the hanging drops and flash-vitrified in liquid nitrogen.
1127 Diffraction data were recorded at 100 K on the Proxima-2A beamline at the Soleil
1128 synchrotron (Paris, France). Native crystals were soaked in I3C using the I3C phasing kit (Hampton
1129 Research), and the dataset was phased using the multiple wavelength anomalous dispersion method.
1130 The diffraction data from the crystals soaked with I3C were collected at 12.67 keV and 5.00 keV. The
1131 structure of the arm segment protein was determined using the program SHELXD[112]. The native
1132 diffraction data recorded from the crystals of arm segment protein were phased using the program
1133 Phaser[113], and the structure was determined using the anomalous data as a molecular replacement
1134 model. Refinement was performed manually using the program *Coot*[114] and automatically in
1135 *REFMAC5*[115]. The structures were validated using *MolProbity*[116].
1136
1137 **Structure determination and refinement using cryo-EM maps**

1138 The structures of phage proteins were predicted using the program Alphafold2[52] and fitted into their
1139 densities as rigid bodies or by individual domains using the programs Chimera[117] or ChimeraX[118], and
1140 then refined interactively using ISOLDE[119]. The structures were improved using the real-space
1141 refinement implemented in the *Phenix* package[120], and corrected manually using the programs
1142 *Coot*[114] and ISOLDE[119]. The geometry evaluation of models was performed using *MolProbity*[116]. Map
1143 to model FSC curves were calculated using Comprehensive Validation tool in *Phenix* package[120].
1144
1145 **Visualization and structure analysis**

1146 Chimera[117] and ChimeraX[118] were used to visualize maps and structures. PISA web server[121] was used
1147 to calculate interface areas. Sequences were analyzed using Clustal Omega[122], available via the
1148 EMBL-EBI server[123] and visualized with Jalview[124].
1149
1150 **Cryo-EM of phi812 attached to *S. aureus* cell wall fragments**

1151 *S. aureus* SA 812 was cultured in 100 ml of meat peptone broth (1 g of Lab-Lemco (Difco), 5 g of yeast
1152 extract powder L21 (Oxoid), 10 g of peptone L37 (Oxoid), and 5 g of NaCl were dissolved in distilled
1153 water to a final volume of 1000 ml, and the pH was adjusted to 7.4 using 10 M NaOH) at 37°C until
1154 OD_{600}=0.3. Cells were harvested by centrifugation at 3,000 x *g* for 15 min. The resulting pellet was
1155 resuspended in 80% isopropanol to a final volume of 10 ml, and incubated for 1 h at room
1156 temperature. The suspension was centrifuged at 1,000 x *g* at room temperature for 15 min. The
1157 resulting supernatant was transferred to another tube, and cell wall fragments were harvested by

centrifugation at 20,000 x *g* for 30 min. The resulting pellet was resuspended in 100 µl of the phage buffer and mixed with phi812 at MOI 10, relative to the starting bacterial culture. After 5 min of incubation at room temperature, the sample was applied to a holey carbon-coated copper grid for electron microscopy (R2/1, mesh 200; Quantifoil), blotted and vitrified by plunging into liquid ethane using a Vitrobot Mark IV (FEI), blot force 2, blotting time 2 s. Grids were imaged at a magnification of 17,000 x, using a Tecnai TF20 operated (FEI) under cryogenic conditions and at an acceleration voltage of 200 kV.

Acknowledgments

We gratefully acknowledge the core facilities Cryo-electron microscopy and tomography, Biomolecular Interactions and Crystallography, Proteomics, and Josef Dadok National NMR Centre of CIISB, Instruct-CZ Centre, supported by MEYS CR (LM2023042) and European Regional Development Fund-Project „UP CIISB“ (No. CZ.02.1.01/0.0/0.0/18_046/0015974). We gratefully acknowledge support from the National Institute of Virology and Bacteriology (Program EXCELES, Project ID No. LX22NPO5103) - Funded by the European Union - Next Generation EU and the project New Technologies for Translational Research in Pharmaceutical Sciences /NETPHARM, project ID OP JAC CZ.02.01.01/00/22_008/0004607, which is co-funded by the European Union. This work received funding from ERC Consolidator Grant No. 101043452 to P.P.

Data availability

Cryo-EM maps and structure coordinates were deposited into the Electron Microscopy Data Bank (EMDB) and Protein Data Bank (PDB), respectively, with the following accession numbers: Structure of native phage phi812 tail computed with imposed sixfold symmetry: EMDB-50093 and PDB-9F04. Structures of baseplate core, wedge modules, arms, and baseplate-proximal part of phi812 tail in a native conformation computed with imposed threefold symmetry: EMDB-19968 and PDB-9EUF. Structures of baseplate core, wedge modules, and baseplate-proximal part of phi812 tail in a native conformation computed with imposed threefold symmetry: EMDB-19969 and PDB-9EUG. Structures of baseplate core and wedge modules of phi812 tail in a native conformation computed with imposed threefold symmetry: EMDB-19970 and PDB-9EUH. Structures of baseplate core, wedge modules, arms, and baseplate-proximal part of phi812 tail in a contracted conformation computed with imposed sixfold symmetry: EMDB-19971 and PDB-9EUI. Structures of baseplate core, wedge modules, arm segment, inner tripod complexes, and baseplate-proximal part of phi812 tail in a contracted conformation computed with imposed sixfold symmetry: EMDB-19972 and PDB-9EUJ. Structures of baseplate core, wedge modules, and inner tripod complexes of phi812 tail in a contracted conformation computed with imposed sixfold symmetry: EMDB-19973 and PDB-9EUK. Structure of tail tube of phage phi812 with contracted tail computed with imposed sixfold symmetry: EMDB-50094 and PDB-9F05. Structure of tail sheath of phage phi812 with contracted tail computed with imposed sixfold symmetry: EMDB-50095 and PDB-9F06. Structure of petal and knob domains of the central spike protein of phage phi812 in a native conformation, computed with imposed threefold symmetry: EMDB-19974 and PDB-9EUL. The NMR structure of the cleaver domain of the hub protein was deposited to PDB under the accession number 9EUM. The X-ray structure of the arm segment protein was deposited to PDB under the accession number 9FKO.

Code availability

All custom scripts used during the single-particle data reconstruction are available at https://github.com/fuzikt/starpy.

References

1. Nobrega, F. L. *et al.* Targeting mechanisms of tailed bacteriophages. *Nat. Rev. Microbiol.* **16**, 760–773 (2018).
2. Leiman, P. G. & Shneider, M. M. Contractile Tail Machines of Bacteriophages. in *Viral Molecular Machines* (eds. Rossmann, M. G. & Rao, V. B.) vol. 726 93–114 (Springer US, Boston, MA, 2012).
3. Taylor, N. M. I. *et al.* Structure of the T4 baseplate and its function in triggering sheath contraction. *Nature* **533**, 346–352 (2016).
4. Li, F. *et al.* High-resolution cryo-EM structure of the Pseudomonas bacteriophage E217. *Nat. Commun.* **14**, 4052 (2023).
5. Wang, Z. *et al.* Structure of Vibrio Phage XM1, a Simple Contractile DNA Injection Machine. *Viruses* **15**, 1673 (2023).
6. Yang, F. *et al.* Fine structure and assembly pattern of a minimal myophage Pam3. *Proc. Natl. Acad. Sci.* **120**, e2213727120 (2023).
7. Yang, F., Wang, L., Zhou, J., Xiao, H. & Liu, H. In Situ Structures of the Ultra-Long Extended and Contracted Tail of Myoviridae Phage P1. *Viruses* **15**, 1267 (2023).
8. Yu, R.-C. *et al.* Structure of the intact tail machine of Anabaena myophage A-1(L). *Nat. Commun.* **15**, 2654 (2024).
9. Sonani, R. R. *et al.* An extensive disulfide bond network prevents tail contraction in Agrobacterium tumefaciens phage Milano. *Nat. Commun.* **15**, 756 (2024).
10. Botka, T. *et al.* Lytic and genomic properties of spontaneous host-range Kayvirus mutants prove their suitability for upgrading phage therapeutics against staphylococci. *Sci. Rep.* **9**, 5475 (2019).
11. Kwiecinski, J. M. & Horswill, A. R. Staphylococcus aureus bloodstream infections: pathogenesis and regulatory mechanisms. *Curr. Opin. Microbiol.* **53**, 51–60 (2020).
12. Grunenwald, C. M., Bennett, M. R. & Skaar, E. P. Nonconventional Therapeutics against Staphylococcus aureus. *Microbiol. Spectr.* **6**, (2018).

1228 13. Venturini, C., Petrovic Fabijan, A., Fajardo Lubian, A., Barbirz, S. & Iredell, J. Biological
1229 foundations of successful bacteriophage therapy. *EMBO Mol. Med.* **14**, (2022).
1230 14. Petrovic Fabijan, A. *et al.* Safety of bacteriophage therapy in severe Staphylococcus aureus
1231 infection. *Nat. Microbiol.* **5**, 465–472 (2020).
1232 15. Uyttebroek, S. *et al.* Safety and efficacy of phage therapy in difficult-to-treat infections: a
1233 systematic review. *Lancet Infect. Dis.* **22**, e208–e220 (2022).
1234 16. Pantůček, R. *et al.* The Polyvalent Staphylococcal Phage φ812:Its Host-Range Mutants and
1235 Related Phages. *Virology* **246**, 241–252 (1998).
1236 17. Nováček, J. *et al.* Structure and genome release of Twort-like Myoviridae phage with a
1237 double-layered baseplate. *Proc. Natl. Acad. Sci.* **113**, 9351–9356 (2016).
1238 18. Guerrero-Ferreira, R. C. *et al.* Structure and transformation of bacteriophage A511 baseplate and
1239 tail upon infection of *Listeria* cells. *EMBO J.* **38**, (2019).
1240 19. Taylor, N. M. I., van Raaij, M. J. & Leiman, P. G. Contractile injection systems of bacteriophages
1241 and related systems. *Mol. Microbiol.* **108**, 6–15 (2018).
1242 20. Veesler, D. & Cambillau, C. A Common Evolutionary Origin for Tailed-Bacteriophage Functional
1243 Modules and Bacterial Machineries. *Microbiol. Mol. Biol. Rev.* **75**, 423–433 (2011).
1244 21. Park, Y.-J. *et al.* Structure of the type VI secretion system TssK–TssF–TssG baseplate subcomplex
1245 revealed by cryo-electron microscopy. *Nat. Commun.* **9**, 5385 (2018).
1246 22. Ge, P. *et al.* Action of a minimal contractile bactericidal nanomachine. *Nature* **580**, 658–662
1247 (2020).
1248 23. Weiss, G. L. *et al.* Structure of a thylakoid-anchored contractile injection system in multicellular
1249 cyanobacteria. *Nat. Microbiol.* **7**, 386–396 (2022).
1250 24. Xu, J. *et al.* Identification and structure of an extracellular contractile injection system from the
1251 marine bacterium Algoriphagus machipongonensis. *Nat. Microbiol.* **7**, 397–410 (2022).
1252 25. Desfosses, A. *et al.* Atomic structures of an entire contractile injection system in both the
1253 extended and contracted states. *Nat. Microbiol.* **4**, 1885–1894 (2019).

1254 26. Jiang, F. *et al.* Cryo-EM Structure and Assembly of an Extracellular Contractile Injection System.
1255 *Cell* **177**, 370-383.e15 (2019).
1256 27. Cai, X. *et al.* Atomic structures of a bacteriocin targeting Gram-positive bacteria. *Nat. Commun.*
1257 **15**, 7057 (2024).
1258 28. Eck, M. J. & Sprang, S. R. The Structure of Tumor Necrosis Factor-α at 2.6 Å Resolution. *J. Biol.*
1259 *Chem.* **264**, 17595–17605 (1989).
1260 29. Legrand, P. *et al.* The Atomic Structure of the Phage Tuc2009 Baseplate Tripod Suggests that Host
1261 Recognition Involves Two Different Carbohydrate Binding Modules. *mBio* **7**, (2016).
1262 30. Farenc, C. *et al.* Molecular Insights on the Recognition of a Lactococcus lactis Cell Wall Pellicle by
1263 the Phage 1358 Receptor Binding Protein. *J. Virol.* **88**, 7005–7015 (2014).
1264 31. McCabe, O. *et al.* The targeted recognition of *L actococcus lactis* phages to their polysaccharide
1265 receptors: Receptor binding to lactococcal phage 1358. *Mol. Microbiol.* **96**, 875–886 (2015).
1266 32. Šulák, O. *et al.* A TNF-like Trimeric Lectin Domain from *Burkholderia cenocepacia* with Specificity
1267 for Fucosylated Human Histo-Blood Group Antigens. *Structure* **18**, 59–72 (2010).
1268 33. Myers, C. L. *et al.* Identification of Two Phosphate Starvation-induced Wall Teichoic Acid
1269 Hydrolases Provides First Insights into the Degradative Pathway of a Key Bacterial Cell Wall
1270 Component. *J. Biol. Chem.* **291**, 26066–26082 (2016).
1271 34. Shi, L., Liu, J.-F., An, X.-M. & Liang, D.-C. Crystal structure of glycerophosphodiester
1272 phosphodiesterase (GDPD) from *Thermoanaerobacter tengcongensis* , a metal ion-dependent
1273 enzyme: Insight into the catalytic mechanism: Crystal Structure of GDPD. *Proteins Struct. Funct.*
1274 *Bioinforma.* **72**, 280–288 (2008).
1275 35. Browning, C., Shneider, M. M., Bowman, V. D., Schwarzer, D. & Leiman, P. G. Phage Pierces the
1276 Host Cell Membrane with the Iron-Loaded Spike. *Structure* **20**, 326–339 (2012).
1277 36. Kanamaru, S. *et al.* Structure of the cell-puncturing device of bacteriophage T4. *Nature* **415**,
1278 553–557 (2002).
1279 37. Shneider, M. M. *et al.* PAAR-repeat proteins sharpen and diversify the type VI secretion system

1280 spike. *Nature* **500**, 350–353 (2013).

1281 38. Kizziah, J. L., Manning, K. A., Dearborn, A. D. & Dokland, T. Structure of the host cell recognition
1282 and penetration machinery of a Staphylococcus aureus bacteriophage. *PLOS Pathog.* **16**,
1283 e1008314 (2020).

1284 39. Büttner, C. R., Wu, Y., Maxwell, K. L. & Davidson, A. R. Baseplate assembly of phage Mu: Defining
1285 the conserved core components of contractile-tailed phages and related bacterial systems. *Proc.*
1286 *Natl. Acad. Sci.* **113**, 10174–10179 (2016).

1287 40. Leiman, P. G. *et al.* Type VI secretion apparatus and phage tail-associated protein complexes
1288 share a common evolutionary origin. *Proc. Natl. Acad. Sci.* **106**, 4154–4159 (2009).

1289 41. Bateman, A. & Rawlings, N. D. The CHAP domain: a large family of amidases including GSP
1290 amidase and peptidoglycan hydrolases. *Trends Biochem. Sci.* **28**, 234–237 (2003).

1291 42. Sanz-Gaitero, M., Keary, R., Garcia-Doval, C., Coffey, A. & van Raaij, M. J. Crystal structure of the
1292 lytic CHAPK domain of the endolysin LysK from Staphylococcus aureus bacteriophage K. *Virol. J.*
1293 **11**, 133 (2014).

1294 43. Becker, S. C., Foster-Frey, J. & Donovan, D. M. The phage K lytic enzyme LysK and lysostaphin act
1295 synergistically to kill MRSA. *FEMS Microbiol. Lett.* **287**, 185–191 (2008).

1296 44. Paul, V. D. *et al.* A novel bacteriophage Tail-Associated Muralytic Enzyme (TAME) from Phage K
1297 and its development into a potent antistaphylococcal protein. *BMC Microbiol.* **11**, 226 (2011).

1298 45. Willis, C. *et al.* Insights into the Membrane Interactions of the Saposin-Like Proteins Na-SLP-1 and
1299 Ac-SLP-1 from Human and Dog Hookworm. *PLOS ONE* **6**, e25369 (2011).

1300 46. Lee, J. H. *et al.* Crystal Structure and Functional Studies Reveal that PAS Factor from Vibrio
1301 vulnificus is a Novel Member of the Saposin-fold Family. *J. Mol. Biol.* **355**, 491–500 (2006).

1302 47. Böth, D., Steiner, E. M., Izumi, A., Schneider, G. & Schnell, R. RipD (Rv1566c) from *Mycobacterium*
1303 *tuberculosis* : adaptation of an NlpC/p60 domain to a non-catalytic peptidoglycan-binding
1304 function. *Biochem. J.* **457**, 33–41 (2014).

1305 48. Habann, M. *et al.* Listeria phage A511, a model for the contractile tail machineries of

1306 SPO1-related bacteriophages. *Mol. Microbiol.* **92**, 84–99 (2014).

1307 49. Schaechter, M. *Encyclopedia of Microbiology*. (Elsevier/Academic Press, Amsterdam Boston,

1308 2009).

1309 50. Maxwell, K. L. *et al.* Structural and Functional Studies of gpX of Escherichia coli Phage P2 Reveal a

1310 Widespread Role for LysM Domains in the Baseplates of Contractile-Tailed Phages. *J. Bacteriol.*

1311 **195**, 5461–5468 (2013).

1312 51. Watts, N. R. & Coombs, D. H. Structure of the bacteriophage T4 baseplate as determined by

1313 chemical cross-linking. *J. Virol.* **64**, 143–154 (1990).

1314 52. Jumper, J. *et al.* Highly accurate protein structure prediction with AlphaFold. *Nature* **596**,

1315 583–589 (2021).

1316 53. Leiman, P. G. *et al.* Structure and Location of Gene Product 8 in the Bacteriophage T4 Baseplate.

1317 *J. Mol. Biol.* **328**, 821–833 (2003).

1318 54. van Dalen, R., Peschel, A. & van Sorge, N. M. Wall Teichoic Acid in Staphylococcus aureus Host

1319 Interaction. *Trends Microbiol.* **28**, 985–998 (2020).

1320 55. Xia, G. *et al.* Wall Teichoic Acid-Dependent Adsorption of Staphylococcal Siphovirus and

1321 Myovirus. *J. Bacteriol.* **193**, 4006–4009 (2011).

1322 56. Takeuchi, I. *et al.* The Presence of Two Receptor-Binding Proteins Contributes to the Wide Host

1323 Range of Staphylococcal Twort-Like Phages. *Appl. Environ. Microbiol.* **82**, 5763–5774 (2016).

1324 57. Azam, A. H., Hoshiga, F., Takeuchi, I., Miyanaga, K. & Tanji, Y. Analysis of phage resistance in

1325 Staphylococcus aureus SA003 reveals different binding mechanisms for the closely related

1326 Twort-like phages ϕSA012 and ϕSA039. *Appl. Microbiol. Biotechnol.* **102**, 8963–8977 (2018).

1327 58. Peng, C. *et al.* Silviavirus phage ϕMR003 displays a broad host range against methicillin-resistant

1328 Staphylococcus aureus of human origin. *Appl. Microbiol. Biotechnol.* **103**, 7751–7765 (2019).

1329 59. Cid, M. *et al.* Recognition of the Helical Structure of β-1,4-Galactan by a New Family of

1330 Carbohydrate-binding Modules. *J. Biol. Chem.* **285**, 35999–36009 (2010).

1331 60. Bae, B. *et al.* Molecular Basis for the Selectivity and Specificity of Ligand Recognition by the

Family 16 Carbohydrate-binding Modules from Thermoanaerobacterium polysaccharolyticum ManA. *J. Biol. Chem.* **283**, 12415–12425 (2008).

61. Bradshaw, W. J. *et al.* The structure of the cysteine protease and lectin-like domains of Cwp84, a surface layer-associated protein from *Clostridium difficile*. *Acta Crystallogr. D Biol. Crystallogr.* **70**, 1983–1993 (2014).

62. Buist, G., Steen, A., Kok, J. & Kuipers, O. P. LysM, a widely distributed protein motif for binding to (peptido)glycans. *Mol. Microbiol.* **68**, 838–847 (2008).

63. Šiborová, M. *et al.* Tail proteins of phage SU10 reorganize into the nozzle for genome delivery. *Nat. Commun.* **13**, 5622 (2022).

64. Sciara, G. *et al.* Structure of lactococcal phage p2 baseplate and its mechanism of activation. *Proc. Natl. Acad. Sci.* **107**, 6852–6857 (2010).

65. Kostyuchenko, V. A. *et al.* The tail structure of bacteriophage T4 and its mechanism of contraction. *Nat. Struct. Mol. Biol.* **12**, 810–813 (2005).

66. Zinke, M., Schröder, G. F. & Lange, A. Major tail proteins of bacteriophages of the order Caudovirales. *J. Biol. Chem.* **298**, 101472 (2022).

67. Kudryashev, M. *et al.* Structure of the Type VI Secretion System Contractile Sheath. *Cell* **160**, 952–962 (2015).

68. Ouyang, R. *et al.* High-resolution reconstruction of a Jumbo-bacteriophage infecting capsulated bacteria using hyperbranched tail fibers. *Nat. Commun.* **13**, 7241 (2022).

69. Aksyuk, A. A. *et al.* The tail sheath structure of bacteriophage T4: a molecular machine for infecting bacteria. *EMBO J.* **28**, 821–829 (2009).

70. Maghsoodi, A., Chatterjee, A., Andricioaei, I. & Perkins, N. C. How the phage T4 injection machinery works including energetics, forces, and dynamic pathway. *Proc. Natl. Acad. Sci.* **116**, 25097–25105 (2019).

71. Ge, P. *et al.* Atomic structures of a bactericidal contractile nanotube in its pre- and postcontraction states. *Nat. Struct. Mol. Biol.* **22**, 377–382 (2015).

1358 72. Moody, M. F. Sheath of bacteriophage T4. *J. Mol. Biol.* **80**, 613–635 (1973).

1359 73. Nazarov, S. *et al.* Cryo- EM reconstruction of Type VI secretion system baseplate and sheath distal
1360 end. *EMBO J.* **37**, e97103 (2018).

1361 74. Fraser, A. *et al.* Quantitative description of a contractile macromolecular machine. *Sci. Adv.* **7**,
1362 eabf9601 (2021).

1363 75. Fernandes, S. & São-José, C. Enzymes and Mechanisms Employed by Tailed Bacteriophages to
1364 Breach the Bacterial Cell Barriers. *Viruses* **10**, 396 (2018).

1365 76. Nishima, W., Kanamaru, S., Arisaka, F. & Kitao, A. Screw Motion Regulates Multiple Functions of
1366 T4 Phage Protein Gene Product 5 during Cell Puncturing. *J. Am. Chem. Soc.* **133**, 13571–13576
1367 (2011).

1368 77. Wenzel, S., Shneider, M. M., Leiman, P. G., Kuhn, A. & Kiefer, D. The Central Spike Complex of
1369 Bacteriophage T4 Contacts PpiD in the Periplasm of Escherichia coli. *Viruses* **12**, 1135 (2020).

1370 78. Hu, B., Margolin, W., Molineux, I. J. & Liu, J. Structural remodeling of bacteriophage T4 and host
1371 membranes during infection initiation. *Proc. Natl. Acad. Sci.* **112**, E4919–E4928 (2015).

1372 79. Gillespie, J. J. *et al.* Structural Insight into How Bacteria Prevent Interference between Multiple
1373 Divergent Type IV Secretion Systems. *mBio* **6**, e01867-15 (2015).

1374 80. Wu, X. *et al.* Crystal structure of CagV, the *Helicobacter pylori* homologue of the T4 SS protein
1375 VirB8. *FEBS J.* **286**, 4294–4309 (2019).

1376 81. Xu, Q. *et al.* Structure of the γ- D -glutamyl- L -diamino acid endopeptidase YkfC from *Bacillus*
1377 *cereus* in complex with L -Ala-γ- D -Glu: insights into substrate recognition by NlpC/P60 cysteine
1378 peptidases. *Acta Crystallograph. Sect. F Struct. Biol. Cryst. Commun.* **66**, 1354–1364 (2010).

1379 82. Bhardwaj, A., Walker-Kopp, N., Casjens, S. R. & Cingolani, G. An Evolutionarily Conserved Family
1380 of Virion Tail Needles Related to Bacteriophage P22 gp26: Correlation between Structural
1381 Stability and Length of the α-Helical Trimeric Coiled Coil. *J. Mol. Biol.* **391**, 227–245 (2009).

1382 83. Bhardwaj, A., Molineux, I. J., Casjens, S. R. & Cingolani, G. Atomic Structure of Bacteriophage Sf6
1383 Tail Needle Knob. *J. Biol. Chem.* **286**, 30867–30877 (2011).

1384 84. Najmudin, S. *et al.* Putting an N-terminal end to the Clostridium thermocellum xylanase Xyn10B
1385 story: Crystal structure of the CBM22-1–GH10 modules complexed with xylohexaose. *J. Struct.*
1386 *Biol.* **172**, 353–362 (2010).
1387 85. Sainz-Polo, M. A., González, B., Menéndez, M., Pastor, F. I. J. & Sanz-Aparicio, J. Exploring
1388 Multimodularity in Plant Cell Wall Deconstruction. *J. Biol. Chem.* **290**, 17116–17130 (2015).
1389 86. Bárdy, P. *et al.* Structure and mechanism of DNA delivery of a gene transfer agent. *Nat. Commun.*
1390 **11**, 3034 (2020).
1391 87. Hardy, J. M. *et al.* The architecture and stabilisation of flagellotropic tailed bacteriophages. *Nat.*
1392 *Commun.* **11**, 3748 (2020).
1393 88. Chao, K. L. *et al.* Structure of Escherichia coli O157:H7 bacteriophage CBA120 tailspike protein 4
1394 baseplate anchor and tailspike assembly domains (TSP4-N). *Sci. Rep.* **12**, 2061 (2022).
1395 89. Han, Z. *et al.* Structural insights into a spindle-shaped archaeal virus with a sevenfold
1396 symmetrical tail. *Proc. Natl. Acad. Sci.* **119**, e2119439119 (2022).
1397 90. Tamura, K. *et al.* Surface glycan-binding proteins are essential for cereal beta-glucan utilization by
1398 the human gut symbiont Bacteroides ovatus. *Cell. Mol. Life Sci.* **76**, 4319–4340 (2019).
1399 91. Granell, M., Namura, M., Alvira, S., Kanamaru, S. & van Raaij, M. Crystal Structure of the
1400 Carboxy-Terminal Region of the Bacteriophage T4 Proximal Long Tail Fiber Protein Gp34. *Viruses*
1401 **9**, 168 (2017).
1402 92. Salazar, A. J., Sherekar, M., Tsai, J. & Sacchettini, J. C. R pyocin tail fiber structure reveals a
1403 receptor-binding domain with a lectin fold. *PLOS ONE* **14**, e0211432 (2019).
1404 93. Plattner, M. *et al.* Structure and Function of the Branched Receptor-Binding Complex of
1405 Bacteriophage CBA120. *J. Mol. Biol.* **431**, 3718–3739 (2019).
1406 94. Garcia-Doval, C. & van Raaij, M. J. Structure of the receptor-binding carboxy-terminal domain of
1407 bacteriophage T7 tail fibers. *Proc. Natl. Acad. Sci.* **109**, 9390–9395 (2012).
1408 95. Fokine, A. *et al.* Molecular architecture of the prolate head of bacteriophage T4. *Proc. Natl.*
1409 *Acad. Sci.* **101**, 6003–6008 (2004).

96. Zheng, S. Q. *et al.* MotionCor2: anisotropic correction of beam-induced motion for improved cryo-electron microscopy. *Nat. Methods* **14**, 331–332 (2017).

97. Zhang, K. Gctf: Real-time CTF determination and correction. *J. Struct. Biol.* **193**, 1–12 (2016).

98. Tang, G. *et al.* EMAN2: an extensible image processing suite for electron microscopy. *J. Struct. Biol.* **157**, 38–46 (2007).

99. Zivanov, J. *et al.* New tools for automated high-resolution cryo-EM structure determination in RELION-3. *eLife* **7**, e42166 (2018).

100. Zivanov, J., Nakane, T. & Scheres, S. H. W. Estimation of high-order aberrations and anisotropic magnification from cryo-EM data sets in RELION-3.1. *IUCrJ* **7**, 253–267 (2020).

101. Kimanius, D., Dong, L., Sharov, G., Nakane, T. & Scheres, S. H. W. New tools for automated cryo-EM single-particle analysis in RELION-4.0. *Biochem. J.* **478**, 4169–4185 (2021).

102. Wagner, T. *et al.* SPHIRE-crYOLO is a fast and accurate fully automated particle picker for cryo-EM. *Commun. Biol.* **2**, 1–13 (2019).

103. Bepler, T. *et al.* Positive-unlabeled convolutional neural networks for particle picking in cryo-electron micrographs. *Nat. Methods* **16**, 1153–1160 (2019).

104. Ilca, S. L. *et al.* Localized reconstruction of subunits from electron cryomicroscopy images of macromolecular complexes. *Nat. Commun.* **6**, 8843 (2015).

105. Evangelidis, T. *et al.* Automated NMR resonance assignments and structure determination using a minimal set of 4D spectra. *Nat. Commun.* **9**, 384 (2018).

106. Shen, Y., Delaglio, F., Cornilescu, G. & Bax, A. TALOS+: a hybrid method for predicting protein backbone torsion angles from NMR chemical shifts. *J. Biomol. NMR* **44**, 213–223 (2009).

107. Güntert, P. Automated structure determination from NMR spectra. *Eur. Biophys. J.* **38**, 129–143 (2009).

108. Linge, J. P., Williams, M. A., Spronk, C. A. E. M., Bonvin, A. M. J. J. & Nilges, M. Refinement of protein structures in explicit solvent. *Proteins Struct. Funct. Bioinforma.* **50**, 496–506 (2003).

109. Nederveen, A. J. *et al.* RECOORD: A recalculated coordinate database of 500+ proteins from the

PDB using restraints from the BioMagResBank. *Proteins Struct. Funct. Bioinforma.* **59**, 662–672 (2005).

110. Bhattacharya, A., Tejero, R. & Montelione, G. T. Evaluating protein structures determined by structural genomics consortia. *Proteins Struct. Funct. Bioinforma.* **66**, 778–795 (2007).

111. Kelley, L. A., Mezulis, S., Yates, C. M., Wass, M. N. & Sternberg, M. J. E. The Phyre2 web portal for protein modeling, prediction and analysis. *Nat. Protoc.* **10**, 845–858 (2015).

112. Schneider, T. R. & Sheldrick, G. M. Substructure solution with *SHELXD*. *Acta Crystallogr. D Biol. Crystallogr.* **58**, 1772–1779 (2002).

113. McCoy, A. J. *et al. Phaser* crystallographic software. *J. Appl. Crystallogr.* **40**, 658–674 (2007).

114. Emsley, P., Lohkamp, B., Scott, W. G. & Cowtan, K. Features and development of *Coot*. *Acta Crystallogr. D Biol. Crystallogr.* **66**, 486–501 (2010).

115. Vagin, A. A. *et al. REFMAC*5 dictionary: organization of prior chemical knowledge and guidelines for its use. *Acta Crystallogr. D Biol. Crystallogr.* **60**, 2184–2195 (2004).

116. Williams, C. J. *et al.* MolProbity: More and better reference data for improved all-atom structure validation. *Protein Sci.* **27**, 293–315 (2018).

117. Pettersen, E. F. *et al.* UCSF Chimera—A visualization system for exploratory research and analysis. *J. Comput. Chem.* **25**, 1605–1612 (2004).

118. Meng, E. C. *et al.* UCSF ChimeraX : Tools for structure building and analysis. *Protein Sci.* **32**, e4792 (2023).

119. Croll, T. I. *ISOLDE* : a physically realistic environment for model building into low-resolution electron-density maps. *Acta Crystallogr. Sect. Struct. Biol.* **74**, 519–530 (2018).

120. Liebschner, D. *et al.* Macromolecular structure determination using X-rays, neutrons and electrons: recent developments in *Phenix*. *Acta Crystallogr. Sect. Struct. Biol.* **75**, 861–877 (2019).

121. Krissinel, E. & Henrick, K. Inference of Macromolecular Assemblies from Crystalline State. *J. Mol. Biol.* **372**, 774–797 (2007).

122. Sievers, F. & Higgins, D. G. Clustal Omega for making accurate alignments of many protein

1462 sequences. *Protein Sci.* **27**, 135–145 (2018).

1463 123.Madeira, F. *et al.* Search and sequence analysis tools services from EMBL-EBI in 2022. *Nucleic*

1464 *Acids Res.* **50**, W276–W279 (2022).

1465 124.Waterhouse, A. M., Procter, J. B., Martin, D. M. A., Clamp, M. & Barton, G. J. Jalview Version 2—a

1466 multiple sequence alignment editor and analysis workbench. *Bioinformatics* **25**, 1189–1191

1467 (2009).